GeoHazards

Article

Pseudo-Probabilistic Design for High-Resolution Tsunami Simulations in the Southwestern Spanish Coast

Alejandro González [1,2,*], Marta Fernández [1,3], Miguel Llorente [1], Jorge Macías [2], Carlos Sánchez-Linares [2], Julián García-Mayordomo [1] and Carlos Paredes [3]

[1] Geological Survey of Spain (CN-IGME CSIC), Department of Research and Prospective Geoscience, Rios Rosas 23, 28003 Madrid, Spain; m.fernandez.hernandez@csic.es (M.F.); m.llorente@csic.es (M.L.); julian.garcia@igme.es (J.G.-M.)

[2] Departamento de Análisis Matemático, Estadística e Investigación Operativa y Matemática Aplicada, Facultad de Ciencias, Universidad de Málaga, Campus de Teatinos, 29010 Málaga, Spain; jmacias@uma.es (J.M.); csl@uma.es (C.S.-L.)

[3] Departamento de Ingeniería Geológica y Minera, Escuela de Minas y Energía, Universidad Politécnica de Madrid, Ríos Rosas 21, 28003 Madrid, Spain; carlos.paredes@upm.es

* Correspondence: alexgp@uma.es or a.gonzalez.pino@csic.es

Abstract: The application of simulation software has proven to be a crucial tool for tsunami hazard assessment studies. Understanding the potentially devastating effects of tsunamis leads to the development of safety and resilience measures, such as the design of evacuation plans or the planning of the economic investment necessary to quickly mitigate their consequences. This article introduces a pseudo-probabilistic seismic-triggered tsunami simulation approach to investigate the potential impact of tsunamis in the southwestern coast of Spain, in the provinces of Huelva and Cádiz. Selected faults, probabilistic distributions and sampling methods are presented as well as some results for the nearly 900 Atlantic-origin tsunamis computed along the 250 km-long coast.

Keywords: tsunami, simulation; seismic faults; sobol sampling; pseudo-probabilistic

Citation: González, A.; Fernández, M.; Llorente, M.; Macías, J.; Sánchez-Linares, C.; García-Mayordomo, J.; Paredes, C. Pseudo-Probabilistic Design for High-Resolution Tsunami Simulations in the Southwestern Spanish Coast. *GeoHazards* **2022**, *3*, 294–322. https://doi.org/10.3390/geohazards3020016

Academic Editor: Katsu Goda

Received: 2 March 2022
Accepted: 18 May 2022
Published: 23 May 2022

1. Introduction

As natural hazards, tsunamis are considered amongst the most potentially devastating phenomena [1]. From the mid-nineteenth century to today, advances in technology have expanded the possibilities for the development of preventive safety measures, laying the groundwork for warning operations known as tsunami early warning systems (TEWS). TEWS provide real-time information on the occurrence and characteristics of a seismic event and enable the launching of corresponding action and/or evacuation plans if the alert level so indicates. These systems are composed of quite different elements, from physical seismic and tsunami sensors to empirical relationships derived from historical records and communication and actuation organisations.

An important aspect of the warning process is the estimation of arrival times, wave height and run-up, which have recently been enhanced through tsunami-wave simulation codes [2,3]. The events in Sumatra (2004) and Japan (2011) have prompted the need to deepen our knowledge of the phenomenom of tsunamis in order to design adequate preventive measures. For example, some measures for tsunami risk reduction have focused on the construction of artificial or natural structures near to the shore [4,5]. However, the high economic impact of the construction of physical barriers, in addition to its doubtful reliability when facing large events [4], has made them controversial. In this example and many others, numerical simulations appear to be an essential tool for tsunami impact studies [6]. In recent years, tsunami modeling tools have been significantly enhanced; the precision of the numerical methods have increased, whilst computing times have drastically decreased [7]. TEWS is a tsunami hazard management tool that focuses on the most relevant element to protect, that of human life. However, TEWS cannot prevent property damage, nor do they help to mitigate the aftermath of the tsunami. Therefore, it is a concern, and a challenge, to provide stakeholders with the best possible tools to understand and quantify the damage caused by tsunamis. One of these stakeholders is the insurance sector and in this paper we present numerical modeling and simulation as a tool to quantify the impact of tsunamis. The final objective of the long-term project with the insurance sector in Spain is to estimate the maximum economic cost of a natural hazard of this type that can affect any Spanish coastal area.

In the literature, many authors have employed numerical models to simulate seismic-triggered tsunamis with the aim of gaining knowledge for distinct purposes. Mas et al. [8] designed vulnerability functions for structures using data from the 2004 Sumatra event, launching a single simulation of a six-segment fault. Fragility functions were also developed in the context of aquaculture rafts and eelgrass for the Japan 2011 event [9], involving the running of three different simulations. With respect to economic impact, research for developing loss functions related to marine vessels was also carried out in [10], where one simulation was computed for the 2011 Japan event as well. Pakoksung et al. [11] launched six simulations to estimate the maximum potential damage loss for a hypothetical non-historical event in Okinawa Island. Goda et al. [12] discussed the tsunami risk potential of the strike-slip fault 2018 Sulawesi event, grounding their work in four simulations. Chenthamil et al. [13] predicted the potential run-up and inundation that might occur in a worst-case scenario on the Koodankulam coast, making use of five tsunamigenic events. Their article also contained a preliminary review concerning epicenter sensibility analysis with 28 simulations computed. Probabilistic-oriented studies, termed probabilistic tsunami hazard analysis (PTHA), use several hundreds of computed simulations to provide results with diverse purposes. In [14], structural losses were evaluated by simulating 242 tsunami events with a mesh resolution of 500 m. In [15], a rigorous computational framework was presented to visualize tsunami hazard and risk assessment uncertainty, where 726 simulations were launched for the 2011 Japan event. A more recent study [16] presents a novel PTHA methodology based on the generation of synthetic seismic catalogues and the incorporation of sea-level variation in a Monte Carlo simulation. Its results were derived from 619 simulations, constructed from five faults surrounding the past event in Cádiz, 1755.

To our knowledge, few PTHA studies have been developed in the northeast Atlantic area. In [17], the authors suggest their study is the first PTHA for the NE Atlantic region for earthquake-generated tsunamis. The methodology followed combined probabilistic seismic hazard assessment, tsunami numerical modeling, and statistical approaches. A set of 150 tsunamigenic scenarios were generated and simulated using a linear shallow water approximation and a 30 arc-seconds ($\approx$90 m) resolution GEBCO bathymetry grid without nesting. In [18], the authors performed a preliminary assessment of probabilistic tsunami inundation in the NE Atlantic region. Their approach consisted of an event-tree method that gathered probability models for seismic sources, tsunami numerical modeling, and statistical methods which were then applied to the coastal test-site of Sines, located on the NE Atlantic coast of Portugal. A total of 94 scenarios were simulated using the non-linear SW equations and a nested grid system at 10 m pixel resolution in a single test-site. An innovative and ambitious initiative within this research field was presented as the North-Eastern Atlantic and Mediterranean (NEAM) Tsunami Hazard Model 2018 [19], which aims to provide a probabilistic hazard model focusing on earthquake-generated tsunamis in the entire NEAM region. The hazard assessment was performed in four steps: probabilistic earthquake model, tsunami generation and modeling in deep water (performed with the Tsunami-HySEA code), shoaling and inundation, inclusion of a local amplification factor and Green's law, and hazard aggregation in conjunction with uncertainty treatment. The authors of this study stated that, although NEAMTHM18 represents a first action, it cannot be a substitute for detailed hazard and risk assessments at a local scale.

Most of the novel techniques in the field of PTHA are based on the notion of reducing the number of required computational runs with the aid of Gaussian process emulators, which are capable of maintaining good output accuracy and uncertainty quantification. The investigations of Gopinathan et al. [20] and Salmanidou et al. [21] are good examples of this approach, where the former delivered millions of output predictions based on 300 numerically simulated earthquake-tsunami scenarios, and the latter produced 2000 output predictions at each prescribed location, examining 60 full-fledged simulations.

This article takes advantage of the most advanced tsunami computational technology to shed light on seismic-triggered tsunamis and their impact on Spanish coasts. The results presented here are intended to generate information in relation to the estimation of the potential economic impact that tsunamis can cause in Spanish territory.

This research project arises from an arrangement between two public entities: the Spanish Geological Survey (CNIGME-CSIC; hereafter IGME) and the Insurance Compensation Consortium of Spain (CCS). The IGME is a National Centre dedicated to research within the Spanish National Research Council (CSIC, Ministry of Science and Innovation), whilst CCS is a Spanish public business entity related to the insurance sector (Ministry of Economic Affairs and Digital Transformation) which takes responsibility for compensation for damages after certain natural events (such as tsunamis), among other areas of activity. Expertise in the numerical simulation of tsunamis and HPC was provided by the University of Málaga.

Bearing in mind the final objective of the simulations considered in this study, these require to be carried out using high-resolution topographic and bathymetric data, since it is of primary importance to be able to discern particular buildings or areas affected by water waves. A five-meter grid resolution is the best nation-wide, readily available, dataset as provided by the National Geographic Institute (IGN) and was considered suitable for the inundation simulations.

The present work presents results of the 896 inundation simulations computed in the Andalusian Atlantic coast, located in the south-west of the Iberian Peninsula. The "Materials and Methods" section begins by explaining the selection of the simulated faults, together with providing some insights on how to generate the Okada parameters that describe each fault. Subsequently, the resolution and source of the different topobathymetric data used for the simulations are detailed. A pseudo-probabilistic approach to the simulations is then presented, explaining how probabilistic distribution for the uncertainty parameters considered has been determined, along with the sampling procedure. The tsunami-simulation numerical model used, as well as the characteristics of the computational cluster, are described to conclude this section. The "Results" section details the outputs obtained for each previously described subsection . It includes a detailed list of the Okada parameters adopted for the simulations, the probabilistic distributions associated with each random variable accounting for every fault, samples obtained by the chosen sampling technique and inundation maps generated from the numerical results. Finally, the discussion section provides an assessment of the possibilities that the generated data create for future research.

2. Materials and Methods

The general methodology followed to achieve the results presented in this study is summarized in Figure 1.

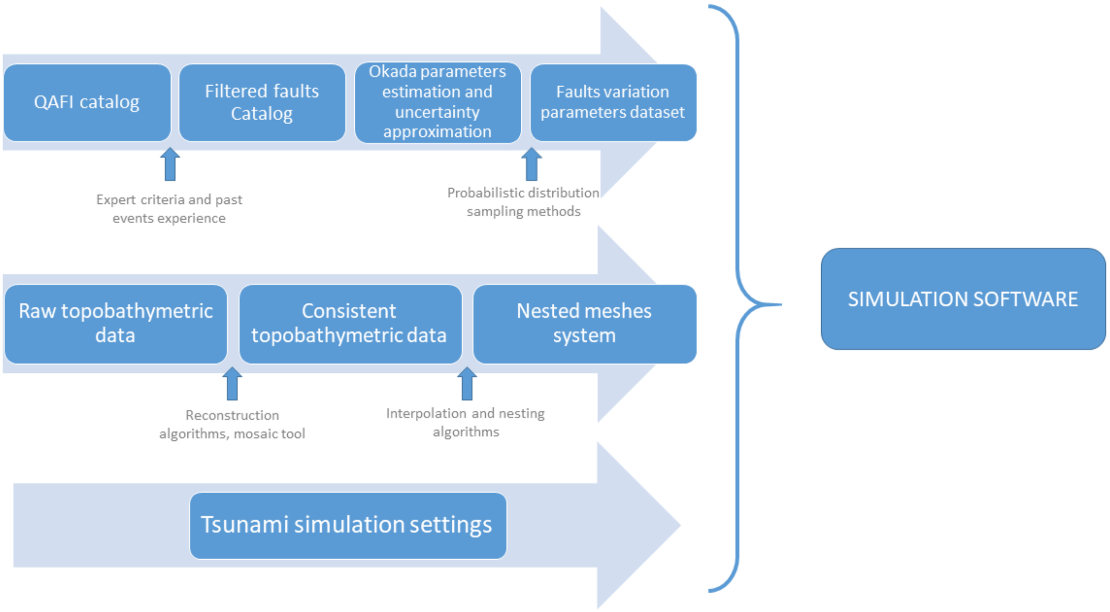

Figure 1. Methodology scheme for this work.

2.1. Tsunami-Triggering Faults

Potential fault sources capable of producing seafloor deformation in SW offshore Iberia were retrieved from the latest version of the QAFI database [22]. The QAFI database compiles information on Quaternary-active faults in the Iberia region both onshore and offshore [23,24]. The database provides basic geometric parameters (e.g., length, strike, dip), as well as a summary of the available evidence of Quaternary activity for each fault. The information compiled in the QAFI database comes chiefly from published sources such as [25–28], among others. A total of 12 faults were selected to be used in this study (Figure 2) after careful review and update of available published information and considering the opinion of a number of experts gathered in a workshop devoted to this task held in 2017 [29]. All the faults considered have published evidence of Quaternary activity, although this activity is very likely but has not yet been definitely demonstrated in the case of the Gorringe Bank (AT001), Guadalquivir Bank (AT002) and Portimao Bank (AT013) faults. Importantly, the so-called Cádiz Wegde Thrust, which some authors assume still involves an ongoing subduction process, was discarded here as there is evidence of inactivity since upper Miocene times [30]. Finally, two additional fault-sources were included to consider potential ruptures comprising two main faults, the Horseshoe and San Vicente (AT005 + AT012) and the Guadalquivir and Portimao (AT002 + AT013) (see Section 3.1).

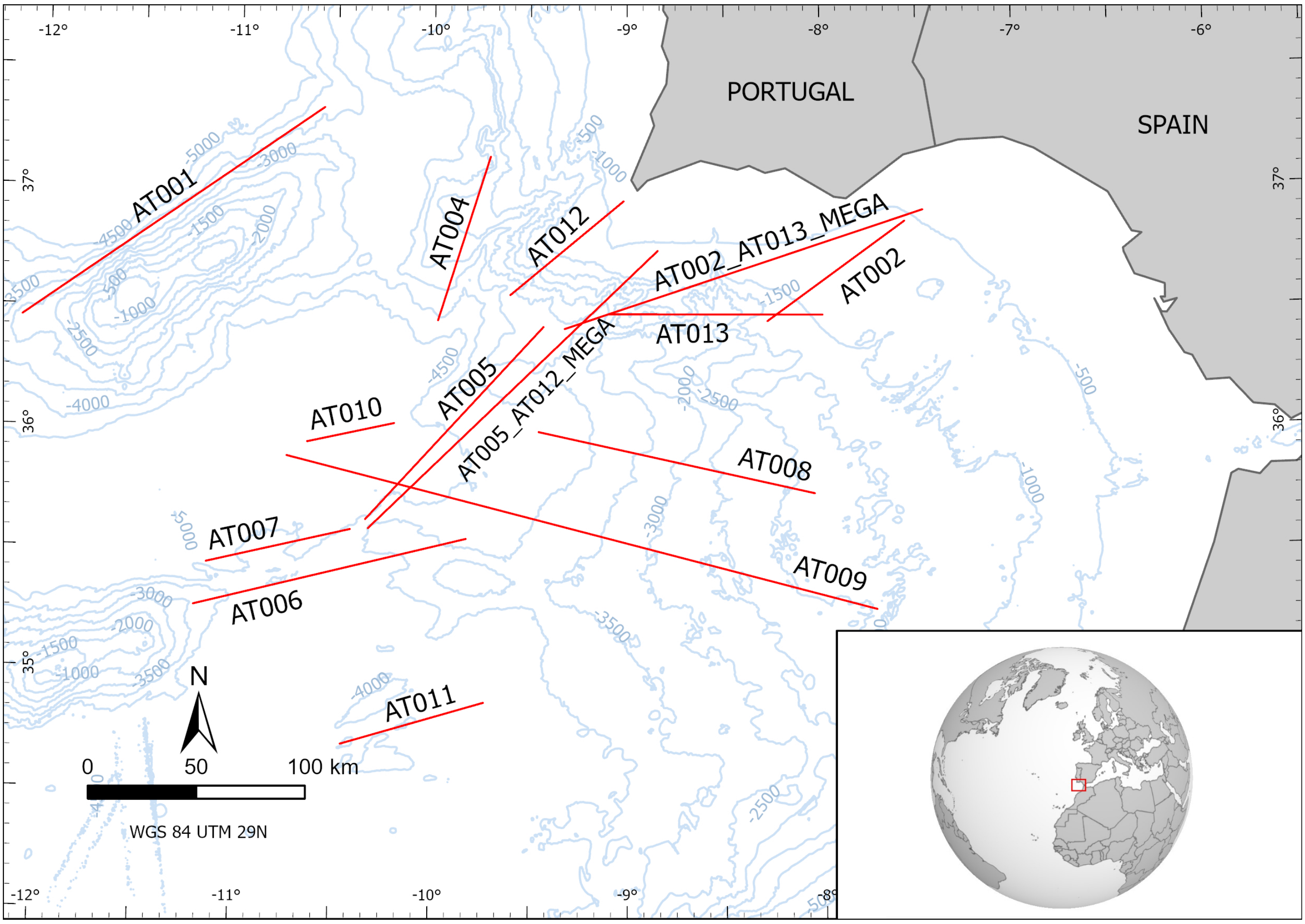

Figure 2. Vector lines corresponding to the tsunamigenic faults considered in this study [22]. The code naming each line corresponds to that used in the QAFI database for cataloguing the faults (Table 1). The suffix 'mega' refers to sources combining two faults.

Table 1. Okada parameters for each of the faults identified as tsunamigenic sources in the southwest of Iberia. The fault code naming corresponds to that used in the QAFI database. The coordinates correspond to the rupture centre of the fault considered as a rectangular shape. All faults are assumed to be composed of one single segment.

QAFI ID	NAME	LON	LAT	DEPTH	LENGTH	WIDTH	STRIKE	DIP	RAKE	SLIP
AT001	Gorringe Bank	−11.348	36.884	25.00	161.0	61.0	60.0	55.0	90.0	3.7
AT002	Guadalqui—vir Bank Thrust	−7.922	36.664	20.00	72.0	80.0	240.0	30.0	90.0	3.0
AT004	Marquês de Pombal	−9.852	36.788	11.50	66.0	56.5	21.0	24.0	90.0	3.0
AT005	Horseshoe	−9.885	36.019	11.50	109.0	46.0	48.0	30.0	90.0	4.0
AT006	Coral Patch South	−10.522	35.392	6.50	127.0	26.0	78.0	30.0	90.0	5.4
AT007	Coral Patch North	−10.786	35.500	6.50	67.0	26.0	79.0	30.0	90.0	2.8
AT008	Lineament North	−8.757	35.859	11.50	130.0	23.1	100.0	85.0	180.0	1.2
AT009	Lineament South	−9.225	35.562	11.50	282.0	23.1	102.0	85.0	180.0	1.7
AT010	Strike Slip 1	−10.432	35.973	11.50	40.0	23.1	80.0	85.0	180.0	0.7
AT011	Seine Hills 3	−10.106	34.771	6.50	66.0	26.0	76.0	30.0	90.0	2.7
AT012	San Vicente Canyon	−9.318	36.754	11.50	63.0	46.0	56.0	30.0	90.0	3.0
AT013	Portimao Bank Thrust	−8.563	36.474	20.00	100.0	80.0	270.0	30.0	90.0	4.2
AT005 + AT012	Horseshoe + San Vicente	−9.596	36.162	11.50	172.0	46.0	52.0	30.0	90.0	6.3
AT002 + AT013	Guadalqui—vir + Portimao	−8.410	36.661	20.00	172.0	80.0	255.0	30.0	90.0	7.4

2.2. Topobathymetric Data Description

The elevation data used for the simulations in the studied area have different resolutions and origins. Concerning emerged terrain elevation data at 5 m pixel resolution, two options were readily available for the project. One option was the data published by the National Geographic Institute (IGN), covering the whole Spanish territory. It can be downloaded from the website [31]. This data was obtained with LIDAR technology and was processed by IGN to derive diverse types of elevation model. The second option was the national Spanish elevation model generated by IGME using IGN's original data, including LIDAR and other IGN archives (such as stereocorrelation photograms at 25 to 50 cm pixels). This elevation model was processed, in particular, to aid in the construction of the National Continuous Geological Map (GEODE), bearing in mind other geological needs. Both models excel in their quality and extent, and may be the best suited for different purposes. Some comparison work carried out between both elevation models indicated that the IGME processing results better represented the geometry of the topographical surface suitable for tsunami simulations since it further cleaned the data of different objects (such as greenhouses, buildings, trees or bridges). This is a critical feature when computing inundation since it prevents most (yet certainly not all) unreal barriers an inundation may face. It is important to note that the IGME model does not include the most up-to-date data from the IGN, as post-processing the entire country at 5 m pixel resolution using the most recent data takes quite a long time and much effort. Therefore, the IGME elevation model at 5 m pixel resolution derived from the IGN data was used, with a granted maximum error 90% lower than 1 m. It should also be noted that the IGME model may present some lower quality results in shadowed slopes than the IGN model because some of the input sources are stereo-imaging in nature—even so, it is more suitable for the purposes of this study but may not be adequate for other approaches or studies.

Regarding submerged topography information (bathymetry), the readily available data comes from different providers at different resolutions and have been obtained by different methods. On the one hand, shallow bathymetry used for the Huelva coast has 20 m pixel resolution, as provided by the Andalusian Environmental Information Network (REDIAM). On the other hand, bathymetric data selected for simulations in the Cádiz region is at 5 m pixel resolution, as provided by the former Ministry of Agriculture, Fisheries and Food (MAPAMA), now the Ministry for Ecological Transition and Demographic Challenge (MITECO). Taking into account that these high-resolution data do not cover the entire region of interest of the project, other sources of information have been used to account for open sea areas and, therefore, to simulate wave propagation. For those regions without high-resolution data, models from the European Marine Observation and Data Network (EMODnet) and The General Bathymetric Chart of the Oceans (GEBCO) at 1/16 arc-minutes ($\approx$115 m) and 15 arc-seconds ($\approx$450 m) pixel resolution, respectively, were used. Both databases are freely available at their respective websites [32,33].

2.3. Pseudo-Probabilistic Approach. Random Variables Distribution and Sobol Sampling Method

Models to simulate tsunamis triggered by seismic events require, in the first instance, to reproduce the initial displacement of the water-free surface produced by the transfer of energy from the movement of the seafloor as a consequence of the fault rupture. As mentioned previously, most commonly accepted and used solutions for co-seismic seabed displacement follow Okada's work [34], which is presented in a relatively simple and analytic form. Then, the static seafloor deformation is directly transmitted to the free surface as an initial condition [35]. Due to the uncertainty related to the determination of the Okada parameters, the simulation of the 14 faults that have been considered for the present study, may be insufficient if the goal is to understand the economic impact that any potential seismic tsunamigenic source of a given probability could produce. Accounting for a given probability is a requirement derived from the EU regulations on insurance after the Solvency II Directive 2009/138/EC. Hence a deterministic approach to unraveling a random problem in nature may not be the best approach to take. An alternative is to account for uncertainty in some of the parameters involved in the seafloor deformation. This idea is the basis of a pseudo-probabilistic study of economic impact. An artificial seismic register is generated by means of the uncertainty associated with some Okada parameters, then each artificial event is simulated and used for the economic impact assessment.

The best case scenario for a pseudo-probabilistic approach would be to consider uncertainty for all the Okada parameters, to the extent that many more different scenarios would be taken into account. However, appropriately exploring a 10-dimensional continuous parameter space for each fault, and consequently simulating every crafted event would implicate a computing power that is currently unattainable or unreasonable costly. If all ten Okada parameters were to be sampled only three times, for both extremes and the average, the amount of combinations to produce an adequate coverage of the input parameter space would increase to 6×10^4, which in turn would boost the simulation needs beyond 10^6 combinations. Moreover, sampling only the extreme values and the average may not appropriately describe the spectrum of damage, considering the highly non-linear issues involved that play a major role. These include wave propagation, wave interaction with the coast and the bathymetry, the elevation data, inundation, and, last but not least, the distribution of elements subject to damage.

As the fault-source modeling employed for this investigation assumes geometric values for which maximum seismic rupture is plausible, parameters, such as dip angle, fault length and width, remain fixed as they illustrate maximum potential values. Furthermore, all faults are assumed to be composed by a single segment. Although variations in segmentation number can have a major impact on inundation results, their assessment would imply adding an Okada parameters list for each segment, thus exponentially increasing the number of possibilities to be combined for a single fault. With respect to the remaining parameters, some tests have been carried out to assess which of them may be described as the driving factors. It is clear that some parameters involve more uncertainty than others, such as strike, rake and slip. For example, although the strike parameter is fairly well-known, it measures fault orientation with respect to the north; thus, minor variations of this orientation could lead to situations where completely different areas become flooded. On the other hand, the rake parameter is chosen to vary to reflect its natural variation along the fault depending on the deflections of the strike with respect to the stress field. Therefore, slip as a random variable is assumed to follow a Gaussian distribution, whilst strike- and rake-associated random variables, due to their circular nature, are considered to follow a Von-Mises distribution.

To reduce the number of scenarios to be simulated, and considering that the resulting economic damage distribution is unknown, such distributions require to be sampled.

In relation to random variable sampling methods, there are several sampling techniques [36], including random-sampling, stratified sampling, Latin hypercube sampling (LHS) and quasi-random sampling with low-discrepancy sequences. Random sampling means that every case of the population has an equal probability of inclusion in the sample. It is a very straightforward method; however, it can lead to a set of gaps or clustering, meaning that there would be some sampled areas overemphasised and some non-sampled areas. Stratified sampling tackles the problem of dividing the input space into strata (or subgroups) and a random sample is taken from each subgroup. This has the advantage of obtaining representation from all the space, although some gaps may still appear. LHS is a type of stratified sampling where each parameter is individually stratified over $s > 2$ levels, such that each level contains the same number of points ([36], p. 76). It can have the advantage of requiring less samples to adequately describe the input space, but this depends on the function to be sampled [37]. Quasi-random sampling sequences are designed to generate samples as uniformly as possible over the unit hypercube. Unlike random numbers, quasi-random points know about the position of previously sampled points, avoiding the appearance of gaps and clusters. One of the best known quasi-random sequences is the Sobol sequences.

The main sampling techniques have been tested in the context of building simulation by MacDonald and Burhenne et al. [37,38], which indicated that the Sobol sequences were superior to LHS, stratified sampling and random sampling in terms of mean convergence speed. In addition, the Sobol sequences method reduced the variability in the cumulative density function, which meant that it was the most robust method among those considered. Burhenne's conclusions were that the Sobol sampling method should be used for building simulation, as the high computational cost requirements for the model make it impossible to run a large number of fully fledged simulations in a reasonable time. It is worth mentioning that the Sobol sequences have already been used successfully in the context of uncertainty quantification of landslide-generated waves [39].

Bearing in mind that the work presented in this paper requires huge computational effort, and in light of the literature reviewed, the Sobol sequences were used as the sampling method to explore the input parametric space considered.

2.4. Simulation Software Tsunami-Hysea and Hpc Resources

The equations most widely accepted by the scientific community to model tsunami wave propagation in the open sea are the nonlinear shallow water equations (NLSWE) [40]. This system of equations comes from a simplification of the Navier–Stokes equations for incompressible and homogeneous fluids, where vertical dynamics can be neglected in comparison to horizontal dynamics, and are set in the framework of a system of hyperbolic partial differential equations.

Nonetheless, NLSWE presents a downside when it comes to model inundation dynamics, since a tsunami wave arriving onshore generates a turbulent regime. Interaction with structures and sediments from the sea deposited on land makes 3D models a necessary tool to accurately simulate these turbulent flow dynamics [41]. In spite of the availability of numerous effective 3D models, they are computationally expensive, rendering it impossible to run complex simulations in a reasonable time or at reasonable cost. Efforts focused on calculating acceleration have included techniques such as adaptative mesh refinement (AMR) [42,43] or multicore parallel computing [44,45]. However, in the last decade, a great paradigm shift occurred in terms of calculation units, with numerical methods traditionally implemented in CPU beginning to be implemented in a graphics processing unit (GPU) environment [46–48], obtaining numerical simulations up to 60 times faster for real events [49].

In this study, the required tsunami simulations were performed using the Tsunami-HySEA code. Tsunami-HySEA is a numerical propagation and inundation model focused on tsunamis that was developed by the EDANYA group at Málaga University in Spain. It implements most advanced finite volume methods, combining robustness, reliability and precision on a single model based on GPU structure, allowing simulation faster than real time. Tsunami-HySEA has been widely tested [50–54] and has also been validated and verified following the standards of the National Tsunami Hazard and Mitigation Program (NTHMP) of the US [55–57]. One key feature implemented in this numerical model is the possibility of using two-way nested meshing for high-resolution simulations. The nested mesh system approach allows computing of open ocean and offshore wave propagation using meshes of lower pixel resolution since the wave length is so long that the minimum number of points needed to adequately capture its form can extend to several kilometres. Near the coast, however, the wavelength is sufficiently small that higher pixel resolution meshes are used, both to reproduce its shape and to capture complex inundation features.

The simulation setup is described as follows. First, the Okada parameters are provided for every scenario. An open boundary condition is assumed on water boundaries, the Manning coefficient is set to 0.03, which is considered a good average value for natural bed roughness, the simulation time is set to 4 h, and the output variables are maximum water height, maximum velocity and maximum mass flow. Each simulation consist of a four-level nested mesh configuration that will be detailed in the next section.

To launch all the simulations, large computational resources are required. Today, high-performance computing (HPC) centers exist all over the world and provide HPC resources for scientific applications, which can be requested and accessed by researchers. These simulations were launched in the Barcelona Supercomputing Center (BSC) cluster, located in Barcelona (Spain). The specifications of this cluster are as follows:

- Linux Operating System and an Infiniband interconnection network.
- 2 login node and 52 compute nodes, each of them:
  - 2 × IBM Power9 8335-GTH @ 2.4 GHz (3.0 GHz on turbo, 20 cores and 4 threads/core, total 160 threads per node)
  - 512 GB of main memory distributed in 16 dimms × 32 GB @ 2666 MHz
  - 2 × SSD 1.9 TB as local storage
  - 2 × 3.2 TB NVME
  - 4 × GPU NVIDIA V100 (Volta) with 16 GB HBM2
  - Single Port Mellanox EDR
  - GPFS via one fiber link 10 GBit

Each simulation was computed on a single GPU.

3. Results

In this section, a description of the numerical results obtained in the present study is provided. First, the complete set of the seismic sources used for the simulations is given. Then, the nested mesh configuration used for the numerical simulations is described. Later, the assignment of probabilistic distributions and the Sobol sampling process are described. Finally, this section concludes with a description of the numerical results that have been obtained.

3.1. Faults List

Figure 2 shows the distribution of the tsunamigenic fault-sources considered in this study and described in Section 2.1. They correspond to complex faults compiled in the QAFI database but are modeled here as rectangular shapes from their basic geometric parameters: length, width, dip and strike (Table 1). The slip was determined from the seismic moment equation [58] considering the rupture area of the fault from the length and width, and a shear modulus that varies between 30, 40 and 60 GPa for faults in the continental crust, oceanic crust or exhumed mantle, respectively. The seismic moment was previously calculated from its relation with the moment magnitude according to Hanks and Kanamori [59]. The moment magnitude was estimated from the empirical relationships recommended in Stirling et al. [60].

3.2. Nested Meshes Spatial Configuration and Resolutions

A set of four levels of nested meshes was considered to carry out the present inundation study at very high resolution along the Andalusian Atlantic coast. The computational domain is covered by the ambient mesh with a numerical resolution of 640 m per pixel, spanning from 34.28° N to 37.49° N and from 12.05° W to 5.5° W. Next, three levels of grids were nested, considering 3 meshes of 160 m pixel resolution, 10 meshes of 40 m pixel resolution and 43 meshes of 5 m pixel resolution that finally shaped the coverage of all areas of interest at high resolution. Figures 3 and 4 show spatial configuration of the meshes. The areas not covered by the highest resolution meshes did not contain sufficient elements of interest for the purposes of this study, but should be included in future revisions if further urbanisation were to be undertaken.

Each 5 m pixel resolution mesh covers an area of 37 km^2, and each 40 m pixel resolution mesh covers an area of 515 km^2. The number of control volumes are the following:

- Each 5 m pixel resolution mesh: $1144 \times 1208 = 1{,}381{,}952$ volumes.
- Each 40 m pixel resolution mesh: $388 \times 784 = 304{,}192$ volumes.
- Upper 160 m pixel resolution mesh: $204 \times 512 = 104{,}448$ volumes.

- Middle 160 m pixel resolution mesh: 384 × 372 = 142,848 volumes.
- Bottom 160 m pixel resolution mesh: 284 × 488 = 138,592 volumes.
- 640 m pixel resolution mesh: 480 × 980 = 470,400 volumes.

The total size of the computational problem to be solved for every single simulation, if they were performed as a single simulation, is quite large, composed of 63,322,144 volumes.

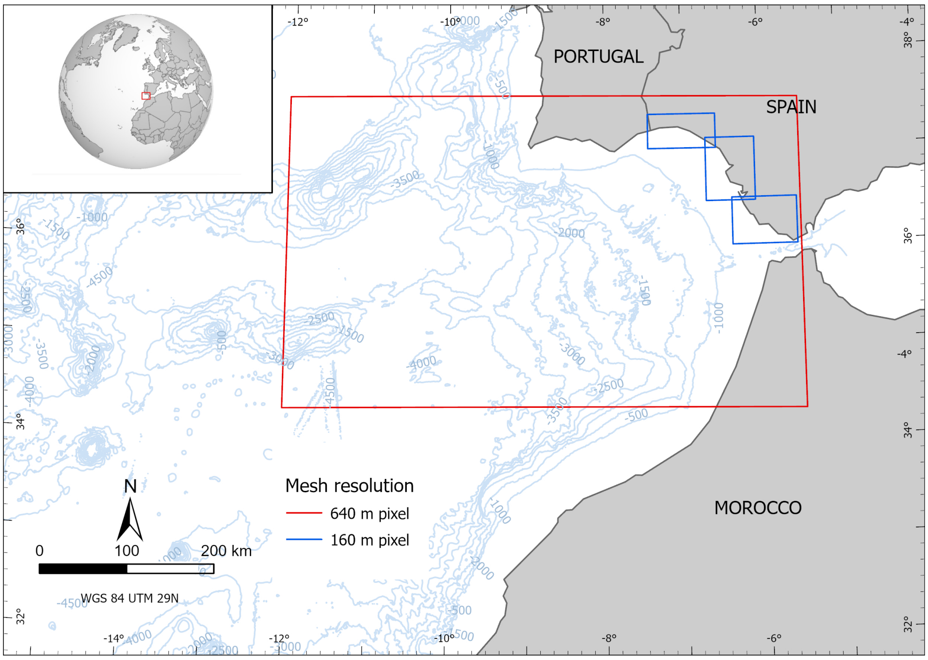

Figure 3. Boundaries of meshes at 640 m and 160 m pixel resolution. The red rectangle delimits the simulation domain boundary, coinciding with the 640 m pixel resolution mesh. Blue rectangles indicate the extension of the three meshes at 160 m pixel resolution.

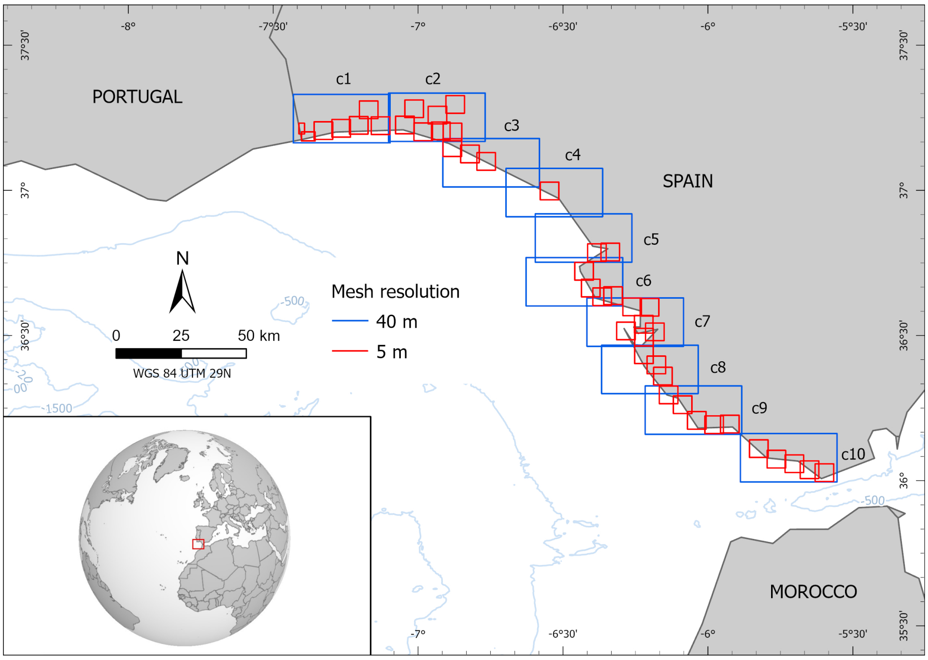

Figure 4. Boundaries of meshes at 40 m and 5 m pixel resolution. Blue rectangles (termed as c1, . . . , c10, from top left to bottom right) indicate the extension of the ten meshes at 40 m pixel resolution. Red rectangles indicate the extension of the 43 meshes at 5 m pixel resolution.

3.3. Assigning Probabilistic Distributions and the Sobol Sampling Process

As previously mentioned, the strike and rake parameters are assumed to follow a Von-Mises distribution, while the slip parameter follows a normal distribution. Given the fact that the available processed data that provide information on the uncertainty of these three parameters is only related to the mean (μ) and the standard deviation (σ), some intermediate work is necessary to adequately describe each fault's Von-Mises parameters. The process is represented as follows.

Recall that the Von-Mises (VM) distribution of the mean μ and the dispersion κ, denoted as $VM(\mu, \kappa)$, has similar properties to the linear normal distribution. To estimate the Von-Mise distribution parameters of a circular random variable using mean and standard deviation sample values, conversion to radian units is first necessary. On the one hand, the mean value of the sample is used for the VM distribution straightforwardly. On the other hand, the standard deviation requires a different treatment, since it has to be adapted to the VM dispersion parameter, κ. Under certain conditions, the parameter κ can be considered as the inverse of the variance, $\kappa = \frac{1}{\sigma^2}$ [61]. The way to relate σ with κ has to do with the first trigonometric moment of the VM distribution [62]. First define the quantity $\rho = e^{-\frac{\sigma^2}{2}}$ (related to dispersion of circular random variable) and then solve

$$\rho = \frac{I_1(\kappa)}{I_0(\kappa)}, \tag{1}$$

where $I_p(\kappa)$ is the modified Bessel function of the first kind and p the order evaluated in κ. The equation (1) can be approximated using the maximum likelihood estimate κ^* of κ, which yields a piecewise function of ρ (see [63], pp.85–86) defined as

$$\kappa^* = \begin{cases} 2\rho + \rho^3 + \frac{5}{6}\rho^5 & , \quad \rho \leq 0.53 \\ -0.4 + 1.39\rho + \frac{0.43}{1-\rho}, & 0.53 \leq \rho < 0.85 \\ \frac{1}{3\rho - 4\rho^2 + \rho^3} & , \quad \rho \geq 0.85 \end{cases}$$

This procedure allows establishing of the well-defined Von-Mises probabilistic distribution for the strike and rake parameters. Table 2 shows the different probabilistic distributions assigned by applying the described procedure.

Table 2. For each of the faults considered in this study, probabilistic distributions associated with the parameter uncertainty is included. In the strike and rake distributions, the first parameter represents the mean in radian units.

	Strike	**Rake**	**Slip**
AT001	$VM(1.05, 525.75)$	$VM(1.57, 8.73)$	$N(3.68, 1.52)$
AT002	$VM(4.19, 131.81)$	$VM(1.57, 8.73)$	$N(3.02, 1.25)$
AT004	$VM(0.37, 525.75)$	$VM(1.57, 33.33)$	$N(3.01, 1.25)$
AT005	$VM(0.84, 525.75)$	$VM(1.57, 33.33)$	$N(3.98, 1.65)$
AT006	$VM(1.36, 525.75)$	$VM(1.57, 33.33)$	$N(5.37, 2.22)$
AT007	$VM(1.38, 525.75)$	$VM(1.57, 33.33)$	$N(2.79, 1.16)$
AT008	$VM(1.75, 3283.31)$	$VM(3.14, 33.33)$	$N(1.21, 0.5)$
AT009	$VM(1.78, 1459.53)$	$VM(3.14, 33.33)$	$N(1.75, 0.72)$
AT010	$VM(1.4, 3283.31)$	$VM(3.14, 33.33)$	$N(0.69, 0.29)$
AT011	$VM(1.33, 33.33)$	$VM(1.57, 33.33)$	$N(2.75, 1.14)$
AT012	$VM(0.98, 525.75)$	$VM(1.57, 33.33)$	$N(3.03, 1.25)$
AT013	$VM(4.71, 131.81)$	$VM(1.57, 8.73)$	$N(4.23, 1.76)$
AT002 + AT013	$VM(4.45, 131.81)$	$VM(1.57, 8.73)$	$N(7.37, 3.06)$
AT005 + AT012	$VM(0.91, 525.75)$	$VM(1.57, 33.33)$	$N(6.35, 2.59)$

Once the probabilistic distributions have been constructed, the procedure used to sample the three-dimensional input space of each fault using the Sobol sequence technique is described below.

1. Select a fixed number of samples N. The number of samples should be a power of 2 due to properties of the Sobol sequences, i.e., $N = 2^m$, $m \in \mathbb{N}$. We choose $N = 64$.
2. Generate a Sobol sequence of size N in three-dimensional unit cube. This will return a three-dimensional sequence with coordinates (x_1, x_2, x_3), each one inside the interval $[0, 1]$.
3. Each coordinate x_i is used to sample the corresponding parameter, i.e., x_1 for strike, x_2 for rake and x_3 for slip. The way to obtain the sample is through the use of the inverse transform sampling method (see [64], p. 28).
4. Now that each coordinate x_i is associated with its corresponding sample s_i, the tuple (s_1, s_2, s_3) is chosen for the simulation.

The Appendix A includes five tables detailing the sampled values using this procedure according to the probabilistic distributions specified in Table 2. Extracting 64 samples expresses that each fault has 64 associated variations, adding a total of $64 \times 14 = 896$ synthetically generated events.

3.4. Numerical Simulations

A total of 896 simulations were launched in the BSC cluster. The simulation runtime was around 4 h for each simulation. As mentioned before, the simulation outputs were maximum water height, maximum velocity and maximum mass flow at each 5 m resolution pixel, producing a 30 MB NetCDF file each. A total amount of 1.1 TB data was generated. Among the data contained in the entire constructed database, some results have been processed and represented to demonstrate how uncertainty in the fault-source parameters affects flood distribution. The illustrations depicted come from simulations of faults AT002 and AT013, as their epicenter locations are closer to the western coast of Andalusian. In order to exemplify the uncertainty in flood distribution, considering the uncertainty associated with the 64 variants of these faults, maximum water height data were prepared for two of the 40 m sub-grids, namely, c1 and c7. The inspection consists of counting how many times each land-located pixel of the 5 m grids contained within the 40 m grids has been wet, in consideration of the 64 fault variants. Each pixel counting is then transformed into relative flood uncertainty levels by application of the Weibull-like function

$$f(i) = 1 - \frac{i}{n+1},$$

where i accounts for the number of times the pixel has been wet and n is the number of fault variants ($n = 64$). Figures 5 and 6 show the results obtained. Figure 5 displays the relative flood uncertainty behaviour with respect to the 64 variants of fault AT013 inside the 40 m grid termed as c1. It is remarkable how the areas surrounding the diverse rivers are prone to be flooded, with flood uncertainty increasing as we move away from the river courses, in contrast to the poor penetration found through *Playa de Bruno* and *Playa Punta del Moral*, which display high levels of uncertainty. Although that is not the case for the beach on the far right side region.

Moving on to the other area, Figure 6 shows the relative behavior of the flood uncertainty with respect to the 64 variants of the AT002 fault within the 40 m grid termed as c7. It is still remarkable how flooding affects the river course's surroundings, with low levels of uncertainty mainly found at the eastern rivers in *Parque Natural de la Bahía de Cádiz*. However, greater flood penetration can be seen along the coast, particularly along the western side of the city of Cádiz and in the bay coast adjacent to *Puerto Real*, where higher flood uncertainty is expected across some sections. In particular, the high-uncertainty area along the western coast of the city of Cádiz and the isthmus is mainly driven by variant 62, as is shown in Appendix B. Both figures illustrate regions with low and high relative flood uncertainty. Low-uncertainty regions (blue) can be interpreted as being more independent of the uncertainty in the fault-source parameters, whereas high-uncertainty regions (violet) only get flooded under a very specific configuration in the source or by concrete sources.

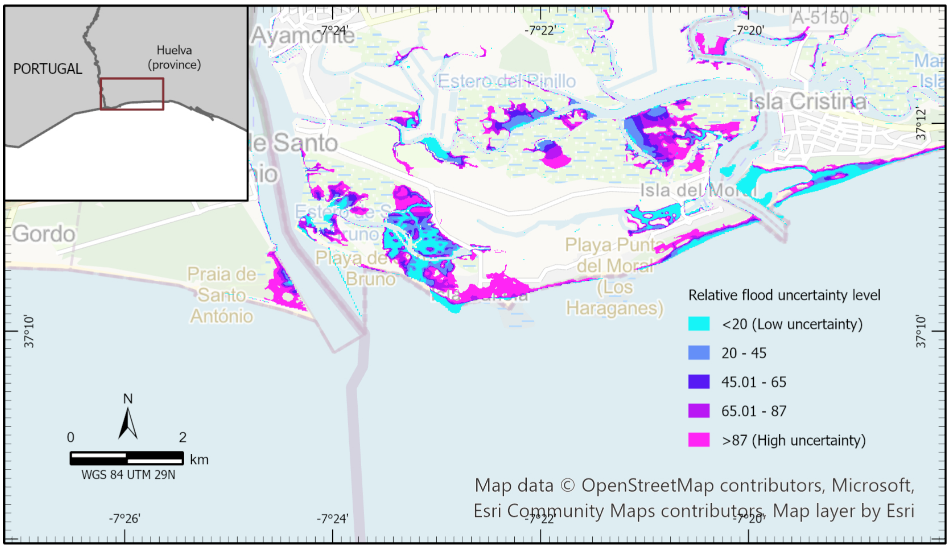

Figure 5. Relative flood uncertainty levels inside the 40 m-grid c1 for the 64 variants of fault AT013.

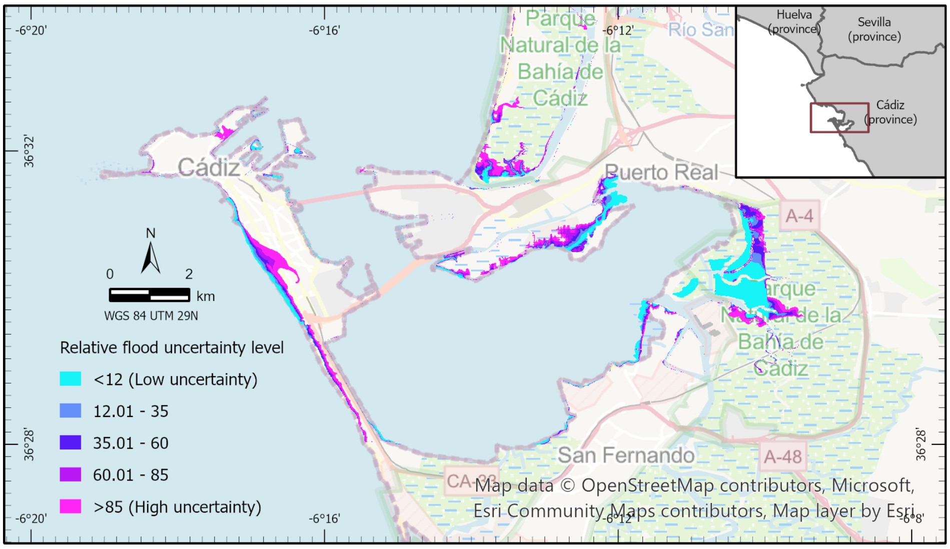

Figure 6. Relative flood uncertainty levels inside the 40 m-grid c7 for the 64 variants of fault AT002.

In addition to the flood-uncertainty figures, some results concerning the maximum water depth, maximum current velocity and maximum mass flow are presented. These results were compiled to fully harness the computational resources reserved for the project at the BSC cluster, and keeping in mind their usefulness for future research. Nonetheless, the data regarding the maximum current velocity and maximum mass flow are not of particular interest for the purpose of the final product, since the estimate of the economic damage will be performed using the data of the maximum water height. Furthermore, isolated results such as these do not contain enough useful information to derive any compelling conclusion; it is necessary to look at all the simulation results to fully understand the underlying phenomena.

Next, the same faults and regions as before are considered, i.e., faults AT002 and AT013, but now we focus on the results concerning variant 37. Variant 37 was chosen because it presents the maximum slip value sampled for both faults. Figure 7 shows three maps including the aforementioned output variables in the 5 m sub-grids placed inside the c1 grid. Figure 8 displays similar data describing the results for the 5 m sub-grids placed inside the c7 grid. Both sets of figures show a slight land inundation. This is an excellent example of why the moment magnitude (related to the slip-rate value) is not the only active factor in terms of a widening in the flooded area, since, for example, variant 62 has a lower slip value but the inundated area is larger (see Appendix B). Although the results presented in this section only account for data collected on some of the 5 m grids, they provide some insight into how uncertainty in the fault-source parameters affects wave propagation. This examination has been undertaken and pointed out in Appendix B.

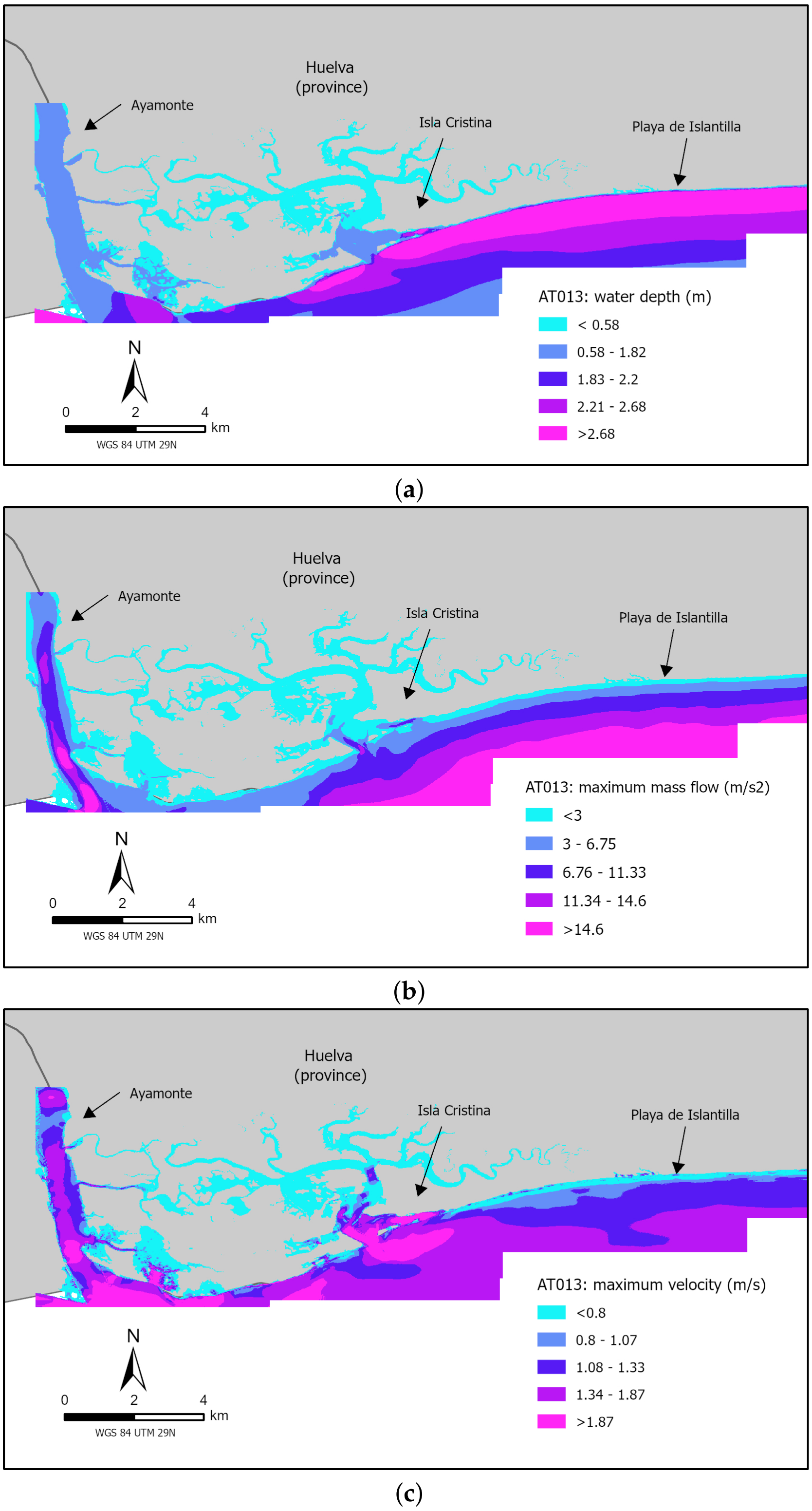

(**a**)

(**b**)

(**c**)

Figure 7. Spatial representation of results obtained for the 5m sub-grids inside the 40 m-grid c1 due to variant 37 of fault AT013 for maximum water depth (**a**) maximum velocity (**b**) and maximum mass flow (**c**).

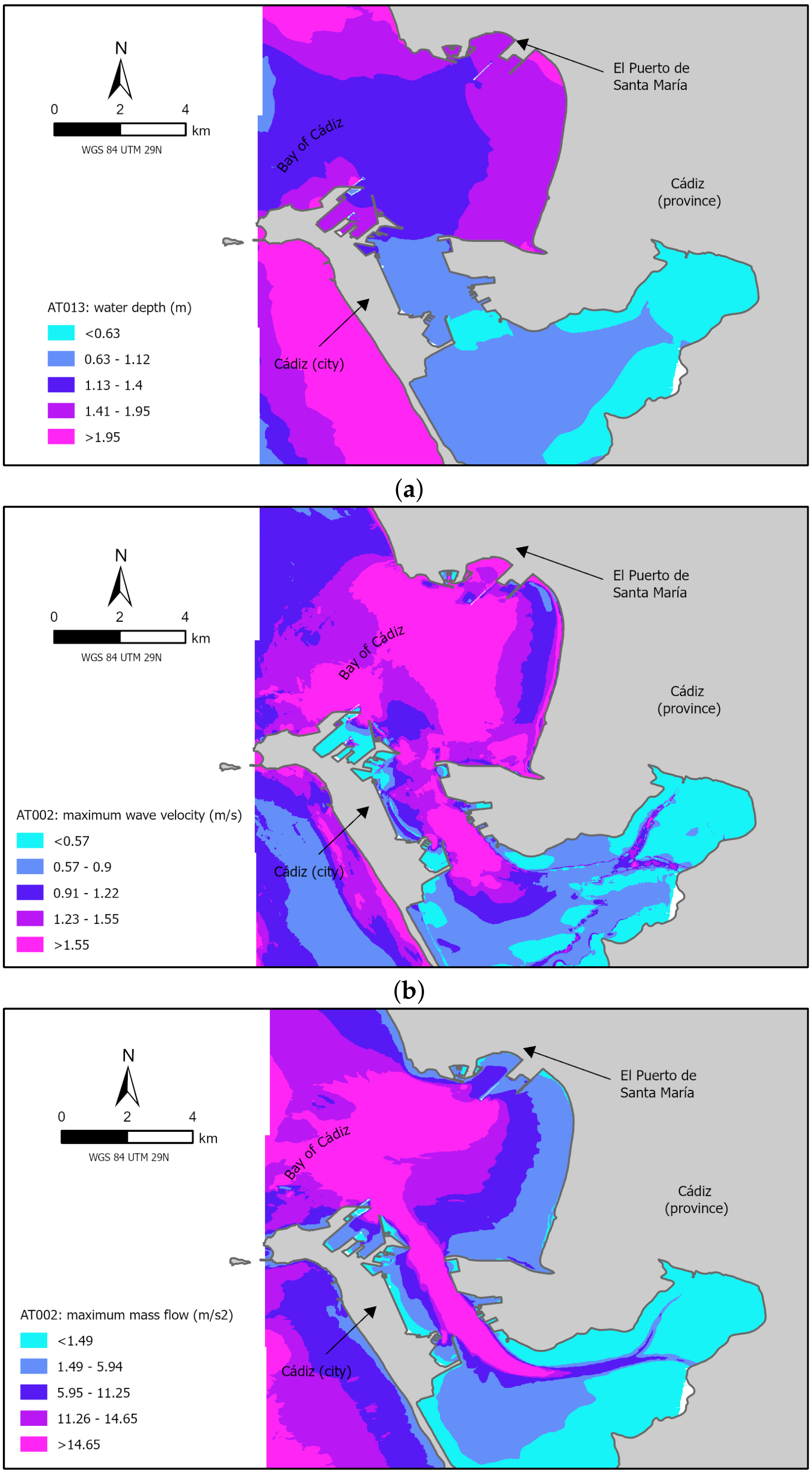

(**a**)

(**b**)

(**c**)

Figure 8. Spatial representation of results obtained for the 5 m sub-grids inside the 40 m-grid c7 due to variant 37 of fault AT002 for maximum water depth (**a**), maximum velocity (**b**) and maximum mass flow (**c**).

4. Discussion

The most recent advances in the field of tsunami hazard assessment research have been progressively oriented towards two main areas of study: scenario-based tsunami hazard analysis (STHA) and probabilistic tsunami hazard analysis (PTHA). One technique or the other is used depending on whether the objective of a project is to design evacuation plans, including evacuation routes, or to analyze various consequences related to damage. Regarding this topic, most of the literature is populated by STHA methods, which take advantage of few simulations to address the consequences of what is generally called "the worst case scenario"—namely, a theoretical unlikely devastating event. The focal point of some of these studies is reproducing past events from historical records for which inundation maps are generated based on intensity measures, such as water heights or run-up [11,13,65–67]. In contrast to STHA, PTHA is a relatively new area of tsunami hazard research. Its foundations were formally established in 2006 with the pioneering work of Geist and Parsons [68], which was grounded in a probabilistic seismic hazard analysis approach. The need to consider the uncertainties involved in seismic-triggered tsunami events, together with the enhancement in computing power, has steadily led to establishing PTHA as the standard viewpoint in this matter [14–19,68–70]. This novel vision in dealing with problems of this nature is founded on the motivation to account for part of the inherent uncertainty in the entire generation-propagation-inundation process of a tsunami event. The key idea in the procedure is to avoid the limitations derived from considering a small set of potential catastrophes, and to produce a catalogue of varied events with the intention of reaching some conclusions in light of all the possible scenarios. The primary results deriving from these investigations are generally directed at risks, commonly related to insurance, or stochastic inundations maps. Moreover, by virtue of assigning fixed return periods to the phenomena (normally seismic ones), probability exceedance maps can be derived, in which the water height or current velocities information delivered is linked to the occurrence probabilities. In this study, we provide a major insight into why the deterministic reference frameworks mentioned above may fail to adequately identify the worst case scenario, since the non-linearity of all elements may lead to the worst consequences far from the largest seismic occurrence. A probabilistic view is difficult, but it is attainable today, and should be the way forward. The methodology followed throughout our work could be placed intermediately between STHA and PTHA. We have shown how to design a synthetic inventory of tsunamigenic events without explicitly prescribing return periods to them. Although we have not produced results comparable with other PTHA studies, what is comparable is the process of building the synthetic inventory. A common way to reconstruct this database consists of fixing some of the Okada parameters and using any sampling strategy to obtain the remaining parameters. Another methodology commonly found in the literature considers randomly distributed heterogeneous slip models [15,70], where several variants of an archetypal slip model are linked to a single fault in a process where the fault is divided into multiple subfaults and a random-generated slip is designated to each one of them. Then, the co-seismic seafloor deformation is calculated empirically from the slip and spatial distribution of the constructed subfaults, providing the initial water elevation by a simple one-on-one translation. This alternative practice for generating the database is a powerful tool when the activity is focused on the underlying uncertainties across complex fault rupture mechanisms. In the context of the previous way of building the database just described, some authors (such as González et al. [16] and Zamora et al. [69]) have designed probable seismic ruptures aiming to cover a wide variety of moment magnitude values. In [16], parameters such as strike, rake and dip remain fixed, while the main effort is concentrated on sampling a seismic moment cumulative density function and thereafter generating slip and fault area size values using some empirical relations. In [69], the authors adopt Gutenberg–Richter's law to estimate b-values, annual earthquake rate and maximum moment magnitude with the purpose of sampling events that incorporate a significant range of seismic moments with respect to predetermined exceedance probabilities. Additionally, they use uniform and normal distributions, as well as empirical relationships to estimate the rest of the geometric parameters. In [71], the artificially crafted register is undertaken via a movement along the fault trace of what the authors termed a typical fault, which is a fault with pre-established Okada parameters in a determined source zone. The González et al. and Zamora et al. approximations have the advantage of generating events that cover a wide spectrum of seismic magnitude, thus indirectly taking into account a large limit of slip values (according to the seismic moment scalar equation [58]). We are aware that either increasing seismic moment or slip values can lead to amplification in the run-up, thus widening the flooded section. Our perspective adds uncertainty directly to the slip variable, without examining the seismic moment directly. Furthermore, we also acknowledge that the moment magnitude or slip rate are not the only variables that play an important role in understanding flood distribution, in as much as the fault segmentation number or the fault-plane dimensions may strongly contribute to it. As mentioned in Section 2.3, this work is based on fault models with the number of segments set to 1, while the fault-plane dimensions and dip angle remain fixed as well. Therefore, in order to capture differences in fault orientation and strike deviations from the stress field, we have emphasized the variability in strike and rake parameters.

In addition to the treatment of uncertainty already mentioned, it is also worth noting the high-resolution simulations that have been carried out and on which this work is based, together with the large extension of the coast that has been covered. The final objective of this project is to examine all the Spanish coasts. In the literature, authors state that, depending on the territory of study and on the local authorities, the available elevation data may or may not be adequate for the final objectives of the project. In [69], the authors use a single 1 arc-min resolution bathymetry to compute the propagation, and then, using some techniques such as Green's Law, they project wave height at some offshore locations towards the coastline. They state that formulas such as Green's Law are needed today because accurate modeling of the tsunami propagation and coastal impact over high-resolution nearshore bathymetry is not yet feasible for regional-scale PTHA, due to high computing resource requirements when targeting hundreds of thousands of seismic scenarios. Their concerns are justified as their inundation modeling is over 4000 km-long, making accurate data acquisition a major issue. Our study, however, is intended to grasp knowledge about inundation in a country-scale scenario and is committed to high-resolution grids in a pseudo-probabilistic scope, meaning that tens of thousands of simulations are being undertaken, covering a 2000 km-long coast. The numerical results presented here represent only a small part of the full picture we are elaborating. The aforementioned statement about infeasibility could derive from factors of limited time, limited computational resources, or even limited high-resolution elevation data collected; however, in general, we believe that, if suitable data are already available, in combination with sufficient HPC resources, the most recent tsunami codes are able to reproduce high-resolution inundation for country-scale dimensions in a matter of months. Even so, it is common knowledge that expensive computational resources for an accurate PTHA study are the main downside. Recent work aimed at circumventing this problem makes use of stochastic approximations, called emulators, built upon a pre-computed training set [20,21,39]. An emulator can be seen as an interpolating operator of the map that assigns to each input parametric array its corresponding desired output through a fully fledged simulation. The emulator encompasses the whole generation, propagation and inundation process without explicitly computing, thus allowing output predictions and uncertainty quantification at fairly low computational cost. The effectiveness of an emulator approach is closely related to the construction of the training set, which is its core. In [20], the epicenter location and moment magnitude were sampled using the LHS method to simulate 300 scenarios and retrieve the maximum water height and maximum current velocity at several locations, which in turn constitute the basis for building the training set. In [21], the authors sampled a seven-dimensional input space using a sequential design MICE algorithm to generate a training set of 60 simulated scenarios. Their sampling technique outperforms the LHS method in the sense that one-shot random sampling for the training set lacks the information acquisition achieved by the sequential design. One-shot methods, such as LHS, can overemphasize unnecessary regions and consequently waste computational resources. On the other hand, the sequential design takes into account the previously computed quantities to select the next input parameters for the next simulation batch.

Finally, recalling the grid resolution, other studies found in the literature reach highest resolution grid pixel sizes of 5 m, 10 m, 50 m, 52 m, 90 m, 93 m [8–13,15–18]. Probabilistic-oriented studies, such as [14,15], run many simulations, but either use a relatively coarse mesh (50 m and 500 m, resp.) or the affected area is relatively small, such as the studies centered only on Tohoku Island. An exception to these studies is the aforementioned emulator-oriented approach [20,21], where the highest resolution grid pixel sizes are 10 m and 30 m, respectively.

5. Conclusions

The methodology adopted in this study follows the general first-step framework in a PTHA environment, where a synthetic seismic catalogue is required to proceed with the subsequent examination. Furthermore, this study could be fully encompassed in the PTHA field if return periods and a logic-tree were added. Even without the probabilistic treatment arising from a potential attachment of return periods, the numerically computed database derived in this study regarding wave height, maximum velocity and maximum mass flow provides an excellent starting point to assess different tsunami-hazard-related issues, such as designing vulnerability functions, developing loss functions or evaluating structural losses (e.g., [8–10,14]).

In particular, our objectives are aimed at drawing conclusions about the economic-related damage distribution caused by a theoretical but plausible tsunamigenic event. In practice, we will determine economic damage due to a specific variation of a single fault in a specific region by overlaying the maximum water height data with the building-scale data in the insurance field. Based on the maximum height of the water column recorded on a single pixel containing any type of construction, an economic value will be associated with it due to a preselected vulnerability function. Adding together the pixel-scale damage estimates for all covered locations will deliver a mapping that links every fault variation to a singular value representing its potential economic damage. By repeating the indicated procedure for the variations of each fault, a probabilistic distribution of the economic damage will be naturally generated, which will be further analyzed. The damage distribution function may have little to do with the largest triggered magnitudes, or the damage may even not be concentrated around the largest flood-likely areas. Direct damage is only possible with the coalescence of any sort of valuable elements (such as people, property, services) with the consequent impact of the phenomena. Such direct damage may then be responsible for further indirect losses (due to the topological and dependent construction of human societies). Considering that neither valuable items nor the value itself are uniformly distributed, in addition to the fact that what is insured, and up to how much, is also unevenly allocated, a probabilistic approach makes more sense to better understand the final damage curve distribution. The most likely damage estimation in terms of monetary loss for the insurance sector cannot be evaluated without considering the full extent of uncertainties in the source and their effects in flooding valuable assets. The results of this work show that some areas are less influenced by the uncertainty in the triggering mechanisms, whereas other areas will only get flooded under a very specific set of triggering conditions. If we only account for one of those sets (a scenario-based approach), it is unclear whether the resulting damage belongs to the most likely output of the many uncertain initial conditions or is actually a representative event of the outcome considering variations in the initial conditions. This method contributes to a better understanding of the damage function, providing crucial and non-pre-existing information for the insurance sector to make better-informed decisions.

Concerning other applications, water height data can also be exploited to understand nearshore and onshore flood distribution from an arbitrary tsunami of Atlantic origin, facilitating the production of stochastic inundations maps and evacuation routes for people living near the coast. Additional information regarding maximum velocity and maximum mass flow can undoubtedly be useful in approaching the evaluation of particular structural damage.

We would like to highlight the importance of the results of this article concerning the numerous computed numerical simulations in conjunction with their high-resolution discretization, where each simulation has produced relevant information for the outstanding population nucleus placed alongside the Atlantic Andalusian coast in building-scale detail.

Future research with reference to this topic should aim to exploit the generated database in search of building-related information of interest in the field of PTHA. The extra work required to achieve these objectives would undeniably be worth the immense enhancement in people's safety and tsunami risk management by regional and local authorities.

Author Contributions: Conceptualization, M.L.; methodology, A.G., J.M., C.S.-L., J.G.-M. and C.P.; literature review, A.G., J.M. and J.G.-M.; supervision, M.L., J.M. and C.S.-L.; visualization, M.F. and M.L.; resources, A.G., J.M., C.S.-L. and J.G.-M.; funding, M.L., J.M.; data curation, A.G. and C.S.-L. All authors have read and agreed to the published version of the manuscript.

Funding: This work has being carried out under a project funded by a public mutual agreement of understanding between the CN-IGME (CSIC) and the CCS (Law reference: BOE 103, 30/04/2019). This project is supported by an agreement of understanding between CN-IGME and UMA, creating a cooperative entity INGEA (Law reference: BOE 332, 22/12/2020). The numerical results presented in this work have been performed with the computational resources allocated by the Spanish Network for Supercomputing (RES) grants AECT-2020-3-0023 and AECT-2021-2-0018. Further support has also been received from the Spanish Government research project MEGAFLOW (RTI2018-096064-B-C21) and ChEESE project (EU Horizon 2020, grant agreement No. 823844, https://cheese-coe.eu/) due to the synergies found between the projects.

Acknowledgments: This work has been carried out with the cooperation of many institutions backing up and helping us in the discussions. Amongst them: IGN, IEO, Civil Protection Authorities (national and regional), ICM-CSIC, IHC, IHM, State Ports, and CEDEX, and several universities, including UA, UGRA, UPM School of Civil Engineering, UCM School of Mining and Energy Engineering, UCM, and UMA.

Conflicts of Interest: The authors declare no conflict of interest.

Abbreviations

The following abbreviations are used in this manuscript:

PTHA	Probabilistic Tsunami Hazard Analysis
STHA	Scenario-based Tsunami Hazard Analysis
PSHA	Probabilistic Seismic Hazard Analysis
VM	Von-Mises
QAFI	Quaternary Active Fault of Iberia
TEWS	Tsunami Early Warning Systems
CCS	Insurance Compensation Consortium of Spain
CSIC	Spanish National Research Council
IGME	Spanish Geological Survey
IGN	National Geographic Institute
GEODE	National Continuous Geological Map
LIDAR	Light Detection And Ranging
REDIAM	Andalusian Environmental Information Network
MITECO	Ecological Transition and Demographic Challenge
EMODnet	European Marine Observation and Data Network
GEBCO	General Bathymetric Chart of the Oceans
LHS	Latin Hypercube Sampling
NLSWE	Non-linear Shallow Water Equations
AMR	Adaptative Mesh Refinement

NTHMP	National Tsunami Hazard and Mitigation Program
HPC	High-Performance Computing
BSC	Barcelona Supercomputing Center
EDANYA	Differential Equations, Mathematical Analysis and Applications

Appendix A. Sobol Sampling Method Results

Results of the sampling technique described in Section 3.3 are presented within this appendix. Tables A1–A5 encapsulate all sampled values used for the subsequent simulations.

Table A1. Sobol sampling results. Each cell numbers are, from top to bottom, strike, rake and slip. Strike and rake units are decimal degrees.

	AT001	AT002	AT004	AT005	AT006	AT007	AT008	AT009	AT010	AT011	AT012	AT013	AT002 + AT013	AT005 + AT012
0	60.0 90.0 3.684	240.0 90.0 3.022	21.0 90.0 3.015	48.0 90.0 3.978	78.0 90.0 5.365	79.0 90.0 2.789	100.0 180.0 1.212	102.0 180.0 1.748	80.0 180.0 0.694	76.0 90.0 2.746	56.0 90.0 3.027	270.0 90.0 4.229	255.0 90.0 7.367	52.0 90.0 6.345
1	61.686 76.69 4.712	243.37 76.69 3.865	22.686 83.277 3.858	49.686 83.277 5.091	79.686 83.277 6.866	80.686 83.277 3.568	100.674 173.277 1.549	103.012 173.277 2.237	80.674 173.277 0.89	82.723 83.277 3.515	57.686 83.277 3.873	273.37 76.69 5.413	258.37 76.69 9.431	53.686 83.277 8.092
2	58.314 103.31 2.655	236.63 103.31 2.179	19.314 96.723 2.172	46.314 96.723 2.866	76.314 96.723 3.865	77.314 96.723 2.01	99.326 −173 0.875	100.988 −173 1.259	79.326 −173 0.499	69.277 96.723 1.977	54.314 96.723 2.181	266.63 103.31 3.046	251.63 103.31 5.303	50.314 96.723 4.598
3	59.204 83.724 4.169	238.408 83.724 3.42	20.204 86.825 3.413	47.204 86.825 4.504	77.204 86.825 6.074	78.204 86.825 3.157	99.681 176.825 1.371	101.522 176.825 1.979	79.681 176.825 0.787	72.825 86.825 3.109	55.204 86.825 3.427	268.408 83.724 4.789	253.408 83.724 8.342	51.204 86.825 7.17
4	62.875 112.804 1.929	245.749 112.804 1.584	23.875 101.479 1.577	50.875 101.479 2.08	80.875 101.479 2.806	81.875 101.479 1.46	101.15 −168 0.637	103.725 −168 0.914	81.15 −168 0.361	87.479 101.479 1.435	58.875 101.479 1.583	275.749 112.804 2.21	260.749 112.804 3.847	54.875 101.479 3.366
5	60.796 67.196 3.198	241.592 67.196 2.624	21.796 78.521 2.617	48.796 78.521 3.453	78.796 78.521 4.656	79.796 78.521 2.421	100.319 168.521 1.053	102.478 168.521 1.517	80.319 168.521 0.602	79.175 78.521 2.383	56.796 78.521 2.627	271.592 67.196 3.67	256.592 67.196 6.392	52.796 78.521 5.52
6	57.125 96.276 5.438	234.251 96.276 4.46	18.125 93.175 4.453	45.125 93.175 5.877	75.125 93.175 7.925	76.125 93.175 4.117	98.85 −176 1.787	100.275 −176 2.582	78.85 −176 1.028	64.521 93.175 4.057	53.125 93.175 4.471	264.251 96.276 6.248	249.251 96.276 10.887	49.125 93.175 9.325
7	57.783 80.366 2.938	235.567 80.366 2.411	18.783 85.13 2.404	45.783 85.13 3.172	75.783 85.13 4.278	76.783 85.13 2.224	99.113 175.13 0.968	100.669 175.13 1.394	79.113 175.13 0.552	67.154 85.13 2.189	53.783 85.13 2.414	265.567 80.366 3.372	250.567 80.366 5.871	49.783 85.13 5.079
8	61.222 107.537 5.036	242.442 107.537 4.131	22.222 98.846 4.124	49.222 98.846 5.442	79.222 98.846 7.339	80.222 98.846 3.813	100.489 −171 1.656	102.733 −171 2.391	80.489 −171 0.951	80.87 98.846 3.757	57.222 98.846 4.14	272.442 107.537 5.786	257.442 107.537 10.082	53.222 98.846 8.643
9	63.835 59.418 3.923	247.669 59.418 3.219	24.835 74.671 3.212	51.835 74.671 4.238	81.835 74.671 5.715	82.835 74.671 2.97	101.534 164.671 1.291	104.301 164.671 1.862	81.534 164.671 0.74	91.329 74.671 2.925	59.835 74.671 3.224	277.669 59.418 4.505	262.669 59.418 7.848	55.835 74.671 6.753
10	59.607 93.097 1.344	239.214 93.097 1.104	20.607 91.567 1.097	47.607 91.567 1.447	77.607 91.567 1.952	78.607 91.567 1.017	99.843 −178 0.445	101.764 −178 0.636	79.843 −178 0.249	74.433 91.567 0.997	55.607 91.567 1.102	269.214 93.097 1.537	254.214 93.097 2.673	51.607 91.567 2.372
11	58.778 72.463 6.023	237.558 72.463 4.94	19.778 81.154 4.933	46.778 81.154 6.51	76.778 81.154 8.779	77.778 81.154 4.56	99.511 171.154 1.979	101.267 171.154 2.861	79.511 171.154 1.139	71.13 81.154 4.495	54.778 81.154 4.952	267.558 72.463 6.922	252.558 72.463 12.062	50.778 81.154 10.319
12	62.217 99.634 3.444	244.433 99.634 2.825	23.217 94.87 2.818	50.217 94.87 3.719	80.217 94.87 5.015	81.217 94.87 2.607	100.887 −175 1.133	103.331 −175 1.634	80.887 −175 0.648	84.846 94.87 2.567	58.217 94.87 2.83	274.433 99.634 3.953	259.433 99.634 6.886	54.217 94.87 5.938
13	60.393 86.903 2.331	240.786 86.903 1.913	21.393 88.433 1.906	48.393 88.433 2.515	78.393 88.433 3.391	79.393 88.433 1.764	100.157 178.433 0.769	102.236 178.433 1.105	80.157 178.433 0.437	77.567 88.433 1.735	56.393 88.433 1.914	270.786 86.903 2.672	255.786 86.903 4.652	52.393 88.433 4.047

Table A2. Sobol sampling results. Each cell numbers are, from top to bottom, strike, rake and slip. Strike and rake units are decimal degrees.

	AT001	**AT002**	**AT004**	**AT005**	**AT006**	**AT007**	**AT008**	**AT009**	**AT010**	**AT011**	**AT012**	**AT013**	**AT002 + AT013**	**AT005 + AT012**
14	56.165 120.582 4.429	232.331 120.582 3.633	17.165 105.329 3.626	44.165 105.329 4.785	74.165 105.329 6.453	75.165 105.329 3.353	98.466 −164 1.457	99.699 −164 2.103	78.466 −164 0.836	60.671 105.329 3.303	52.165 105.329 3.64	262.331 120.582 5.087	247.331 120.582 8.863	48.165 105.329 7.611
15	56.705 88.456 5.224	233.413 88.456 4.284	17.705 89.219 4.277	44.705 89.219 5.645	74.705 89.219 7.612	75.705 89.219 3.955	98.682 179.219 1.717	100.023 179.219 2.481	78.682 179.219 0.987	62.841 89.219 3.897	52.705 89.219 4.295	263.413 88.456 6.002	248.413 88.456 10.458	48.705 89.219 8.961
16	60.593 127.363 3.07	241.185 127.363 2.519	21.593 108.639 2.512	48.593 108.639 3.315	78.593 108.639 4.47	79.593 108.639 2.324	100.237 −161 1.011	102.356 −161 1.457	80.237 −161 0.577	78.363 108.639 2.287	56.593 108.639 2.522	271.185 127.363 3.523	256.185 127.363 6.136	52.593 108.639 5.303
17	62.525 74.667 1.674	245.047 74.667 1.374	23.525 82.26 1.367	50.525 82.26 1.804	80.525 82.26 2.433	81.525 82.26 1.266	101.01 172.26 0.553	103.515 172.26 0.793	81.01 172.26 0.312	86.074 82.26 1.243	58.525 82.26 1.373	275.047 74.667 1.916	260.047 74.667 3.334	54.525 82.26 2.931
18	58.995 101.421 4.045	237.991 101.421 3.318	19.995 95.772 3.311	46.995 95.772 4.37	76.995 95.772 5.893	77.995 95.772 3.063	99.598 −174 1.331	101.397 −174 1.92	79.598 −174 0.763	71.992 95.772 3.016	54.995 95.772 3.325	267.991 101.421 4.646	252.991 101.421 8.093	50.995 95.772 6.959
19	59.804 63.814 3.564	239.608 63.814 2.924	20.804 76.841 2.917	47.804 76.841 3.849	77.804 76.841 5.191	78.804 76.841 2.698	99.922 166.841 1.173	101.882 166.841 1.691	79.922 166.841 0.671	75.219 76.841 2.657	55.804 76.841 2.929	269.608 63.814 4.092	254.608 63.814 7.127	51.804 76.841 6.142
20	64.657 94.671 6.524	249.315 94.671 5.35	25.657 92.363 5.343	52.657 92.363 7.052	82.657 92.363 9.51	83.657 92.363 4.94	101.863 −177 2.143	104.794 −177 3.099	81.863 −177 1.234	94.639 92.363 4.869	60.657 92.363 5.365	279.315 94.671 7.498	264.315 94.671 13.067	56.657 92.363 11.17
21	61.448 82.074 4.567	242.893 82.074 3.746	22.448 85.992 3.739	49.448 85.992 4.934	79.448 85.992 6.654	80.448 85.992 3.457	100.579 175.992 1.502	102.869 175.992 2.168	80.579 175.992 0.862	81.772 85.992 3.406	57.448 85.992 3.754	272.893 82.074 5.246	257.893 82.074 9.139	53.448 85.992 7.845
22	58.059 109.989 2.5	236.121 109.989 2.051	19.059 100.074 2.044	46.059 100.074 2.697	76.059 100.074 3.638	77.059 100.074 1.892	99.224 −169 0.824	100.835 −169 1.185	79.224 −169 0.469	68.26 100.074 1.861	54.059 100.074 2.053	266.121 109.989 2.867	251.121 109.989 4.991	50.059 100.074 4.334
23	57.475 70.011 3.803	234.953 70.011 3.12	18.475 79.926 3.113	45.475 79.926 4.108	75.475 79.926 5.54	76.475 79.926 2.879	98.99 169.926 1.251	100.485 169.926 1.805	78.99 169.926 0.717	65.926 79.926 2.835	53.475 79.926 3.125	264.953 70.011 4.367	249.953 70.011 7.607	49.475 79.926 6.548
24	61.005 97.926 0.843	242.009 97.926 0.693	22.005 94.008 0.687	49.005 94.008 0.905	79.005 94.008 1.221	80.005 94.008 0.637	100.402 −175 0.281	102.603 −175 0.398	80.402 −175 0.154	80.008 94.008 0.622	57.005 94.008 0.689	272.009 97.926 0.96	257.009 97.926 1.667	53.005 94.008 1.521
25	63.295 85.329 2.8	246.587 85.329 2.298	24.295 87.637 2.291	51.295 87.637 3.023	81.295 87.637 4.077	82.295 87.637 2.12	101.318 177.637 0.923	103.977 177.637 1.328	81.318 177.637 0.526	89.159 87.637 2.086	59.295 87.637 2.3	276.587 85.329 3.213	261.587 85.329 5.595	55.295 87.637 4.845
26	59.407 116.186 4.868	238.815 116.186 3.992	20.407 103.159 3.985	47.407 103.159 5.26	77.407 103.159 7.093	78.407 103.159 3.685	99.763 −166 1.6	101.644 −166 2.311	79.763 −166 0.919	73.637 103.159 3.631	55.407 103.159 4.001	268.815 116.186 5.592	253.815 116.186 9.743	51.407 103.159 8.356
27	58.552 78.579 2.143	237.107 78.579 1.759	19.552 84.228 1.752	46.552 84.228 2.312	76.552 84.228 3.118	77.552 84.228 1.622	99.421 174.228 0.707	101.131 174.228 1.016	79.421 174.228 0.401	70.228 84.228 1.595	54.552 84.228 1.759	267.107 78.579 2.457	252.107 78.579 4.277	50.552 84.228 3.729

Table A3. Sobol sampling results. Each cell numbers are, from top to bottom, strike, rake and slip. Strike and rake units are decimal degrees.

	AT001	**AT002**	**AT004**	**AT005**	**AT006**	**AT007**	**AT008**	**AT009**	**AT010**	**AT011**	**AT012**	**AT013**	**AT002 + AT013**	**AT005 + AT012**
28	61.941 105.333 4.297	243.879 105.333 3.525	22.941 97.74 3.518	49.941 97.74 4.642	79.941 97.74 6.26	80.941 97.74 3.253	100.776 −172 1.413	103.165 −172 2.04	80.776 −172 0.811	83.74 97.74 3.205	57.941 97.74 3.532	273.879 105.333 4.935	258.879 105.333 8.598	53.941 97.74 7.387
29	60.196 52.637 5.694	240.392 52.637 4.669	21.196 71.361 4.662	48.196 71.361 6.153	78.196 71.361 8.298	79.196 71.361 4.311	100.078 161.361 1.871	102.118 161.361 2.704	80.078 161.361 1.076	76.781 71.361 4.249	56.196 71.361 4.681	270.392 52.637 6.542	255.392 52.637 11.4	52.196 71.361 9.759
30	55.343 91.544 3.322	230.685 91.544 2.725	16.343 90.781 2.718	43.343 90.781 3.587	73.343 90.781 4.837	74.343 90.781 2.515	98.137 −179 1.094	99.206 −179 1.576	78.137 −179 0.625	57.361 90.781 2.476	51.343 90.781 2.729	260.685 91.544 3.813	245.685 91.544 6.641	47.343 90.781 5.731
31	55.81 77.649 4.107	231.621 77.649 3.369	16.81 83.76 3.362	43.81 83.76 4.437	73.81 83.76 5.983	74.81 83.76 3.109	98.324 173.76 1.351	99.486 173.76 1.95	78.324 173.76 0.775	59.245 83.76 3.063	51.81 83.76 3.376	261.621 77.649 4.717	246.621 77.649 8.217	47.81 83.76 7.064
32	60.294 104.302 1.808	240.588 104.302 1.485	21.294 97.222 1.478	48.294 97.222 1.949	78.294 97.222 2.629	79.294 97.222 1.368	100.118 −172 0.597	102.177 −172 0.857	80.118 −172 0.337	77.173 97.222 1.344	56.294 97.222 1.484	270.588 104.302 2.071	255.588 104.302 3.604	52.294 97.222 3.16
33	62.076 46.507 3.134	244.15 46.507 2.572	23.076 68.415 2.565	50.076 68.415 3.384	80.076 68.415 4.564	81.076 68.415 2.373	100.83 158.415 1.032	103.246 158.415 1.487	80.83 158.415 0.59	84.281 68.415 2.335	58.076 68.415 2.575	274.15 46.507 3.597	259.15 46.507 6.265	54.076 68.415 5.412
34	58.667 90.771 5.327	237.335 90.771 4.369	19.667 90.39 4.362	46.667 90.39 5.756	76.667 90.39 7.763	77.667 90.39 4.033	99.467 −179 1.751	101.2 −179 2.53	79.467 −179 1.007	70.684 90.39 3.974	54.667 90.39 4.379	267.335 90.771 6.12	252.335 90.771 10.664	50.667 90.39 9.136
35	59.507 68.658 2.579	239.015 68.658 2.116	20.507 79.25 2.109	47.507 79.25 2.783	77.507 79.25 3.753	78.507 79.25 1.952	99.803 169.25 0.85	101.704 169.25 1.223	79.803 169.25 0.484	74.036 79.25 1.92	55.507 79.25 2.118	269.015 68.658 2.958	254.015 68.658 5.15	51.507 79.25 4.469
36	63.544 97.094 4.638	247.087 97.094 3.804	24.544 93.588 3.798	51.544 93.588 5.012	81.544 93.588 6.758	82.544 93.588 3.512	101.418 −176 1.525	104.127 −176 2.202	81.418 −176 0.876	90.16 93.588 3.46	59.544 93.588 3.813	277.087 97.094 5.328	262.087 97.094 9.283	55.544 93.588 7.967
37	61.112 84.531 6.968	242.223 84.531 5.714	22.112 87.233 5.707	49.112 87.233 7.532	79.112 87.233 10.158	80.112 87.233 5.276	100.445 177.233 2.289	102.668 177.233 3.31	80.445 177.233 1.319	80.435 87.233 5.201	57.112 87.233 5.73	272.223 84.531 8.009	257.223 84.531 13.958	53.112 87.233 11.924
38	57.633 114.405 3.624	235.269 114.405 2.973	18.633 102.275 2.966	45.633 102.275 3.914	75.633 102.275 5.278	76.633 102.275 2.743	99.053 −167 1.193	100.58 −167 1.72	79.053 −167 0.683	66.558 102.275 2.701	53.633 102.275 2.978	265.269 114.405 4.161	250.269 114.405 7.247	49.633 102.275 6.244
39	58.189 61.79 4.95	236.38 61.79 4.06	19.189 75.84 4.053	46.189 75.84 5.349	76.189 75.84 7.213	77.189 75.84 3.748	99.276 165.84 1.627	100.913 165.84 2.35	79.276 165.84 0.935	68.778 75.84 3.693	54.189 75.84 4.069	266.38 61.79 5.687	251.38 61.79 9.908	50.189 75.84 8.496
40	61.565 93.881 2.87	243.128 93.881 2.355	22.565 91.964 2.348	49.565 91.964 3.098	79.565 91.964 4.178	80.565 91.964 2.172	100.626 −178 0.945	102.939 −178 1.362	80.626 −178 0.539	82.24 91.964 2.138	57.565 91.964 2.358	273.128 93.881 3.293	258.128 93.881 5.735	53.565 91.964 4.964
41	65.385 81.229 1.128	250.775 81.229 0.927	26.385 85.565 0.92	53.385 85.565 1.213	83.385 85.565 1.636	84.385 85.565 0.853	102.154 175.565 0.374	105.231 175.565 0.533	82.154 175.565 0.208	97.585 85.565 0.835	61.385 85.565 0.924	280.775 81.229 1.288	265.775 81.229 2.239	57.385 85.565 2.004

Table A4. Sobol sampling results. Each cell numbers are, from top to bottom, strike, rake and slip. Strike and rake units are decimal degrees.

	AT001	**AT002**	**AT004**	**AT005**	**AT006**	**AT007**	**AT008**	**AT009**	**AT010**	**AT011**	**AT012**	**AT013**	**AT002 + AT013**	**AT005 + AT012**
42	59.902 108.726 3.863	239.804 108.726 3.169	20.902 99.442 3.162	47.902 99.442 4.173	77.902 99.442 5.627	78.902 99.442 2.925	99.961 −170 1.271	101.941 −170 1.834	79.961 −170 0.728	75.61 99.442 2.88	55.902 99.442 3.175	269.804 108.726 4.436	254.804 108.726 7.727	51.902 99.442 6.65
43	59.1 87.681 3.383	238.201 87.681 2.776	20.1 88.827 2.769	47.1 88.827 3.653	77.1 88.827 4.927	78.1 88.827 2.561	99.64 178.827 1.114	101.46 178.827 1.605	79.64 178.827 0.637	72.412 88.827 2.521	55.1 88.827 2.78	268.201 87.681 3.883	253.201 87.681 6.764	51.1 88.827 5.835
44	62.693 123.492 5.846	245.384 123.492 4.794	23.693 106.755 4.787	50.693 106.755 6.318	80.693 106.755 8.52	81.693 106.755 4.426	101.077 −163 1.921	103.616 −163 2.776	81.077 −163 1.105	86.75 106.755 4.362	58.693 106.755 4.806	275.384 123.492 6.718	260.384 123.492 11.706	54.693 106.755 10.017
45	60.694 73.591 4.362	241.387 73.591 3.578	21.694 81.719 3.571	48.694 81.719 4.713	78.694 81.719 6.356	79.694 81.719 3.303	100.278 171.719 1.435	102.417 171.719 2.071	80.278 171.719 0.823	78.767 81.719 3.253	56.694 81.719 3.586	271.387 73.591 5.01	256.387 73.591 8.729	52.694 81.719 7.498
46	56.926 100.516 2.24	233.854 100.516 1.838	17.926 95.316 1.831	44.926 95.316 2.416	74.926 95.316 3.259	75.926 95.316 1.695	98.77 −174 0.739	100.155 −174 1.062	78.77 −174 0.42	63.725 95.316 1.667	52.926 95.316 1.839	263.854 100.516 2.568	248.854 100.516 4.47	48.926 95.316 3.893
47	56.456 75.698 2.729	232.913 75.698 2.239	17.456 82.778 2.232	44.456 82.778 2.945	74.456 82.778 3.972	75.456 82.778 2.065	98.582 172.778 0.899	99.873 172.778 1.294	78.582 172.778 0.513	61.84 82.778 2.032	52.456 82.778 2.241	262.913 75.698 3.131	247.913 75.698 5.451	48.456 82.778 4.724
48	60.493 102.351 4.788	240.985 102.351 3.928	21.493 96.24 3.921	48.493 96.24 5.174	78.493 96.24 6.977	79.493 96.24 3.625	100.197 −173 1.574	102.296 −173 2.274	80.197 −173 0.904	77.964 96.24 3.572	56.493 96.24 3.936	270.985 102.351 5.501	255.985 102.351 9.584	52.493 96.24 8.222
49	62.367 89.229 3.743	244.731 89.229 3.071	23.367 89.61 3.064	50.367 89.61 4.043	80.367 89.61 5.452	81.367 89.61 2.834	100.947 179.61 1.232	103.42 179.61 1.777	80.947 179.61 0.705	85.442 89.61 2.791	58.367 89.61 3.076	274.731 89.229 4.298	259.731 89.229 7.487	54.367 89.61 6.447
50	58.888 133.493 0.399	237.777 133.493 0.33	19.888 111.585 0.323	46.888 111.585 0.425	76.888 111.585 0.573	77.888 111.585 0.301	99.555 −158 0.135	101.332 −158 0.187	79.555 −158 0.069	71.565 111.585 0.291	54.888 111.585 0.324	267.777 133.493 0.449	252.777 133.493 0.776	50.888 111.585 0.767
51	59.706 82.906 5.559	239.412 82.906 4.559	20.706 86.412 4.552	47.706 86.412 6.008	77.706 86.412 8.102	78.706 86.412 4.209	99.882 176.412 1.827	101.823 176.412 2.64	79.882 176.412 1.051	74.827 86.412 4.148	55.706 86.412 4.57	269.412 82.906 6.388	254.412 82.906 11.13	51.706 86.412 9.53
52	64.19 111.342 3.26	248.379 111.342 2.675	25.19 100.75 2.668	52.19 100.75 3.52	82.19 100.75 4.747	83.19 100.75 2.468	101.676 −169 1.073	104.514 −169 1.547	81.676 −169 0.614	92.755 100.75 2.429	60.19 100.75 2.679	278.379 111.342 3.742	263.379 111.342 6.517	56.19 100.75 5.626
53	61.333 65.595 2.04	242.665 65.595 1.675	22.333 77.725 1.668	49.333 77.725 2.201	79.333 77.725 2.968	80.333 77.725 1.544	100.533 167.725 0.673	102.8 167.725 0.967	80.533 167.725 0.382	81.316 77.725 1.518	57.333 77.725 1.675	272.665 65.595 2.338	257.665 65.595 4.07	53.333 77.725 3.554
54	57.924 95.469 4.233	235.85 95.469 3.472	18.924 92.767 3.465	45.924 92.767 4.573	75.924 92.767 6.167	76.924 92.767 3.205	99.17 −177 1.392	100.754 −177 2.009	79.17 −177 0.799	67.719 92.767 3.157	53.924 92.767 3.479	265.85 95.469 4.861	250.85 95.469 8.469	49.924 92.767 7.278
55	57.307 86.119 1.521	234.616 86.119 1.25	18.307 88.036 1.243	45.307 88.036 1.639	75.307 88.036 2.211	76.307 88.036 1.151	98.923 178.036 0.503	100.384 178.036 0.72	78.923 178.036 0.283	65.25 88.036 1.13	53.307 88.036 1.248	264.616 86.119 1.741	249.616 86.119 3.029	49.307 88.036 2.673

Table A5. Sobol sampling results. Each cell numbers are, from top to bottom, strike, rake and slip. Strike and rake units are decimal degrees.

	AT001	**AT002**	**AT004**	**AT005**	**AT006**	**AT007**	**AT008**	**AT009**	**AT010**	**AT011**	**AT012**	**AT013**	**AT002 + AT013**	**AT005 + AT012**
56	60.9 118.21 3.984	241.799 118.21 3.268	21.9 104.16 3.261	48.9 104.16 4.304	78.9 104.16 5.804	79.9 104.16 3.016	100.36 −165 1.311	102.54 −165 1.891	80.36 −165 0.751	79.588 104.16 2.971	56.9 104.16 3.274	271.799 118.21 4.575	256.799 118.21 7.97	52.9 104.16 6.856
57	63.074 71.274 5.127	246.146 71.274 4.205	24.074 80.558 4.198	51.074 80.558 5.541	81.074 80.558 7.472	82.074 80.558 3.882	101.23 170.558 1.686	103.845 170.558 2.435	81.23 170.558 0.969	88.275 80.558 3.825	59.074 80.558 4.215	276.146 71.274 5.891	261.146 71.274 10.264	55.074 80.558 8.797
58	59.306 98.771 3.005	238.613 98.771 2.466	20.306 94.435 2.459	47.306 94.435 3.244	77.306 94.435 4.375	78.306 94.435 2.274	99.722 −175 0.99	101.583 −175 1.426	79.722 −175 0.565	73.233 94.435 2.239	55.306 94.435 2.468	268.613 98.771 3.448	253.613 98.771 6.005	51.306 94.435 5.192
59	58.435 56.508 4.497	236.872 56.508 3.689	19.435 73.245 3.682	46.435 73.245 4.859	76.435 73.245 6.552	77.435 73.245 3.405	99.374 163.245 1.479	101.061 163.245 2.135	79.374 163.245 0.849	69.76 73.245 3.354	54.435 73.245 3.696	266.872 56.508 5.165	251.872 56.508 8.999	50.435 73.245 7.727
60	61.811 92.319 2.417	243.62 92.319 1.984	22.811 91.173 1.977	49.811 91.173 2.608	79.811 91.173 3.517	80.811 91.173 1.829	100.724 −178 0.797	103.087 −178 1.146	80.724 −178 0.453	83.222 91.173 1.799	57.811 91.173 1.985	273.62 92.319 2.772	258.62 92.319 4.826	53.811 91.173 4.194
61	60.098 79.484 3.504	240.196 79.484 2.875	21.098 84.684 2.868	48.098 84.684 3.784	78.098 84.684 5.103	79.098 84.684 2.653	100.039 174.684 1.153	102.059 174.684 1.663	80.039 174.684 0.66	76.39 84.684 2.612	56.098 84.684 2.879	270.196 79.484 4.023	255.196 79.484 7.007	52.098 84.684 6.04
62	54.615 106.409 6.239	229.225 106.409 5.117	15.615 98.281 5.11	42.615 98.281 6.744	72.615 98.281 9.094	73.615 98.281 4.724	97.846 −171 2.05	98.769 −171 2.963	77.846 −171 1.18	54.415 98.281 4.657	50.615 98.281 5.13	259.225 106.409 7.171	244.225 106.409 12.495	46.615 98.281 10.686
63	55.031 84.931 3.474	230.06 84.931 2.85	16.031 87.436 2.843	43.031 87.436 3.752	73.031 87.436 5.059	74.031 87.436 2.63	98.013 177.436 1.143	99.019 177.436 1.649	78.013 177.436 0.654	56.101 87.436 2.589	51.031 87.436 2.854	260.06 84.931 3.988	245.06 84.931 6.946	47.031 87.436 5.989

Appendix B. Uncertainty Visualization in Wave Propagation and Building-Scale Inundation for a Particular Fault-Source Configuration

This appendix is devoted to portraying how the alterations in fault-source parameters considered throughout the article affect wave propagation at several locations in the open sea. In order to proceed with the examination, three virtual buoys have been allocated in the open sea, and one more has been placed closer to the shoreline. Figure A1 shows the studied area as well as the position of the buoys. All buoys belong to a line with latitude of 36.5° N and are numbered from 1 to 4, buoy number 1 being the farthest from the coast and buoy number 4 the closest one. Wave propagation due to rupture of all 64 variants of fault AT002 has been simulated, and a time series regarding the wave amplitude values produced by every fault variant has been constructed with respect to each buoy. Fault AT002 has been chosen because of its proximity to the Cádiz's coast. The simulation time is set to 4 h for every variant; the time series temporal resolution is 1min.

Figure A2 shows wave height variations in all four locations. At first glance, it can be noted how all variants follow a similar trend as to what time peaks are recorded, though peak values may present important discrepancies among variants. Variants 50 and 62 are highlighted in all cases, as they represent extreme behaviours. The fact that these two specific variations display the mentioned behaviour is something to be expected—they come from retrieving extreme slip values in the sampling methods described in Section 3.3. Variant 50 has a slip value of 0.33, whilst variant 62 has a slip value of 5.117 (Tables A4 and A5). Looking at the four graphs, from buoy 1 (furthest) to 4 (closest), it is possible to observe how waves are being propagated, as well as an increase in maximum wave amplitude due to the progressive decrease in water depth.

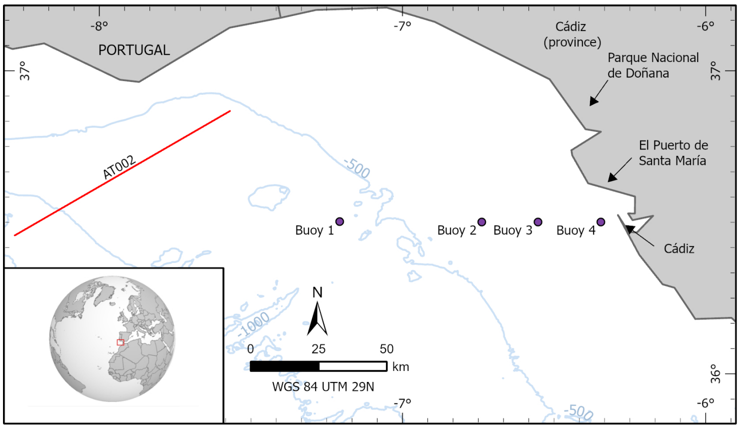

Figure A1. Location of the four virtual buoys together with the simulated fault.

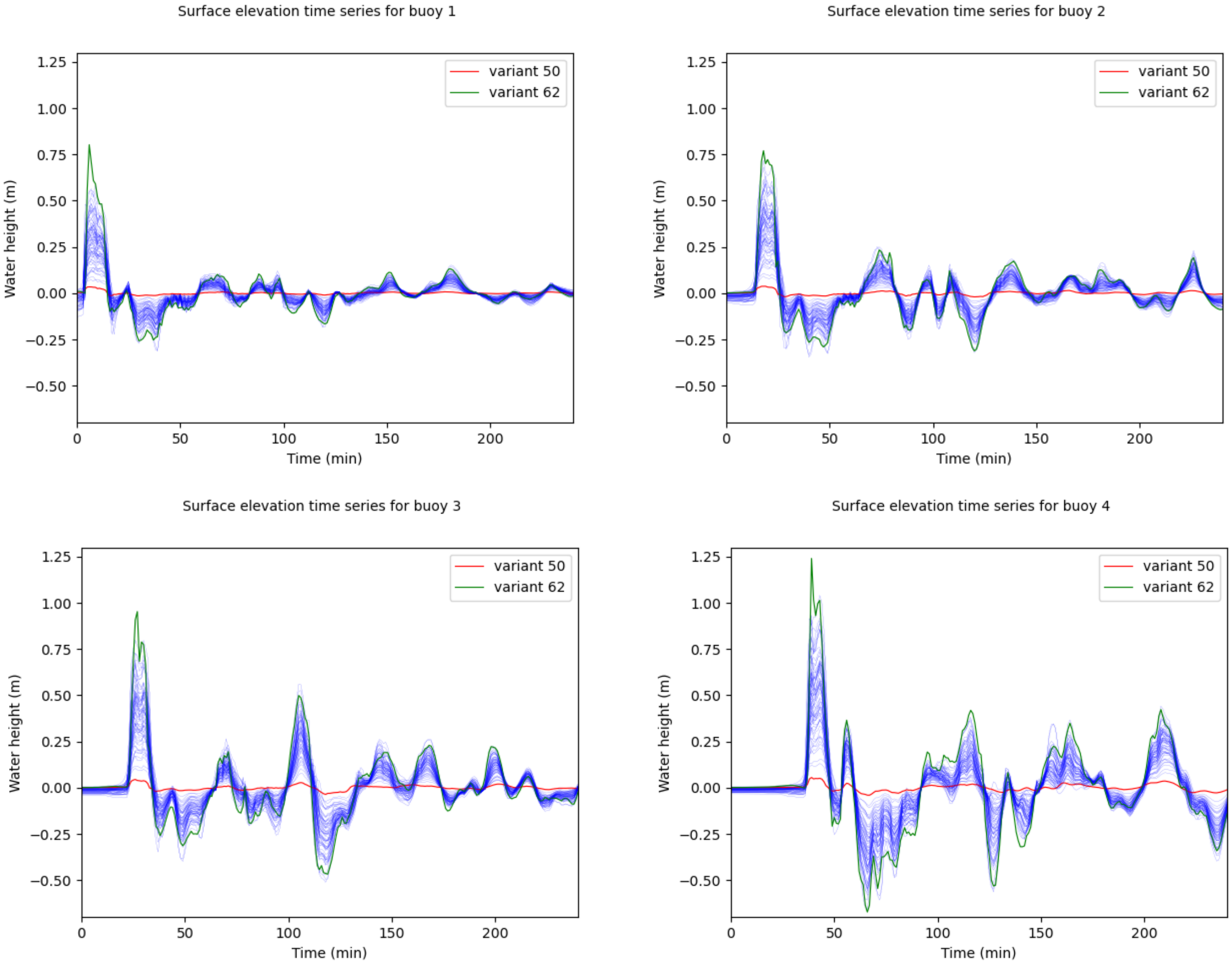

Figure A2. Water elevation time series for each variant of fault AT002 for the four selected fictional buoys. Variants 50 (red) and 62 (green) are highlighted as they display extreme behaviours as to wave amplitude ranges.

To conclude this appendix, a particular result of the water depth is depicted in order to demonstrate how important is the use of high-resolution grids when a study of economic damage is to be undertaken. Variant 62 of fault AT002 is chosen because its particular fault-source parameter configuration provokes a more extensive flood area than other variants in the city of Cádiz. The water depth simulated results are superposed to the street's path. Figure A3 provides a direct visualization of the flooded zones. It can be seen how water penetrates through the western coast, wetting some streets and building with maximum height below 1m. Water depth below 1m is also reached through the northern port. High-resolution inundation, in conjunction with building-scale data, permits the identification of economic damage with relatively high accuracy.

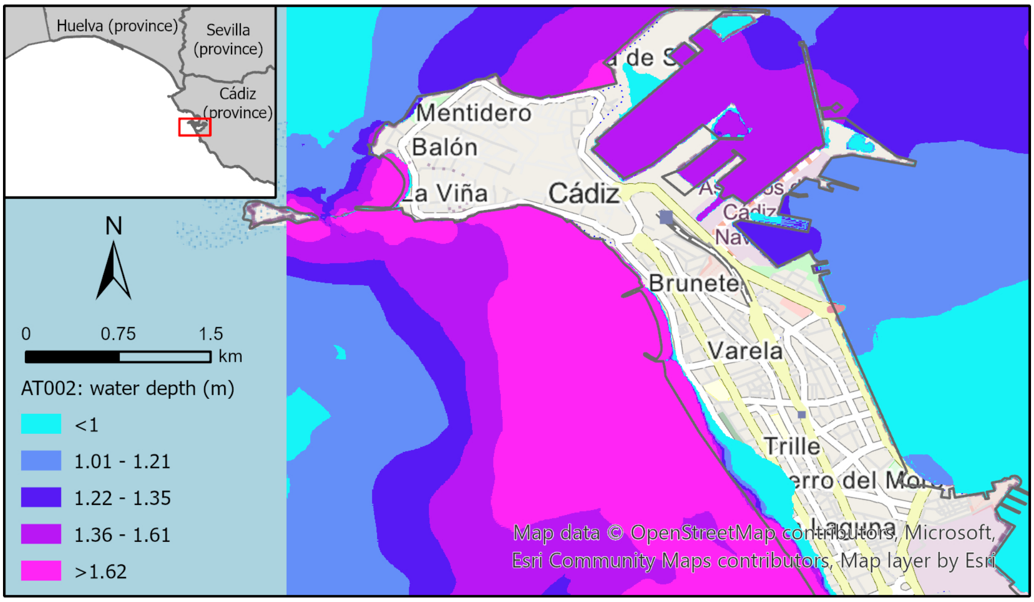

Figure A3. Water depth values obtained by variant 62 of fault AT002 in Cádiz city. Streets have been added to the map in order to visualize how they might be potentially wet by the tsunami wave.

References

1. United Nations Office for Disaster Risk Reduction Documents and Publications Page. Available online: https://www.preventionweb.net/files/64454_unisdrannualreport2018eversionlight.pdf (accessed on 18 February 2022).
2. Liu, P.; Wang, X.; Salisbury, A. Tsunami hazard and early warning system in South China Sea. *J. Asian Earth Sci.* **2009**, *36*, 2–12. [CrossRef]
3. Rudloff, A.; Lauterjung, J.; Münch, U.; Tinti, S. Preface "The GITEWS Project (German-Indonesian Tsunami Early Warning System)". *Nat. Hazards Earth Syst. Sci.* **2009**, *9*, 1381–1382. [CrossRef]
4. Ishiwatari, M.; Sagara, J. World Bank. Available online: http://hdl.handle.net/10986/16160 (accessed on 18 February 2022).
5. Lunghino, B.; Tate, A.F.S.; Mazereeuw, M.; Muhari, A.; Giraldo, F.X.; Marras, S.; Suckale, J. The protective benefits of tsunami mitigation parks and ramifications for their strategic design. *Proc. Natl. Acad. Sci. USA* **2020**, *117*, 10740–10745. [CrossRef] [PubMed]
6. Behrens, J.; Dias, F. New computational methods in tsunami science. *Philos. Trans. R. Soc. A* **2015**, *373*, 20140382. [CrossRef]
7. Marras, S.; Mandli, K.T. Modeling and Simulation of Tsunami Impact: A Short Review of Recent Advances and Future Challenges. *Geosciences* **2021**, *11*, 5. [CrossRef]
8. Mas, E.; Koshimura, S.; Suppasri, A.; Matsuoka, M.; Matsuyama, M.; Yoshii, T.; Jimenez, C.; Yamazaki, F.; Imamura, F. Developing Tsunami fragility curves using remote sensing and survey data of the 2010 Chilean Tsunami in Dichato. *Nat. Hazards Earth Syst. Sci.* **2012**, *8*, 2689–2697. [CrossRef]
9. Suppasri, A.; Fukui, K.; Yamashita, K.; Leelawat, N.; Ohira, H.; Imamura, F. Developing fragility functions for aquaculture rafts and eelgrass in the case of the 2011 Great East Japan tsunami. *Nat. Hazards Earth Syst. Sci.* **2018**, *18*, 145–155. [CrossRef]
10. Muhari, A.; Charvet, I.; Tsuyoshi, F.; Suppasri, A.; Imamura, F. Assessment of tsunami hazards in ports and their impact on marine vessels derived from tsunami models and the observed damage data. *Nat. Hazards* **2015**, *78*, 1309–1328. [CrossRef]
11. Pakoksung, K.; Suppasri, A.; Matsubae, K.; Imamura, F. Estimating tsunami economic losses of Okinawa island with multi-regional-input-output modeling. *Geosciences* **2019**, *9*, 349. [CrossRef]
12. Goda, K.; Mori, N.; Yasuda, T.; Prasetyo, A.; Muhammad, A.; Tsujio, D. Cascading Geological Hazards and Risks of the 2018 Sulawesi Indonesia Earthquake and Sensitivity Analysis of Tsunami Inundation Simulations. *Front. Earth Sci.* **2019**, *7* 261. [CrossRef]
13. Selvan, S. C.; Kankara, R.S. Tsunami model simulation for 26 December 2004 and its effect on Koodankulam region of Tamil Nadu Coast. *Int. J. Ocean. Clim. Syst.* **2016**, *7*, 62–69. [CrossRef]

14. Jaimes, M.; Reinoso, E.; Ordaz, M.; Huerta, B.; Silva, R.; Mendoza, E.; Rodriguez, J. A new approach to probabilistic earthquake-induced tsunami risk assessment. *Ocean Coast Manag.* **2016**, *119*, 68–75. [CrossRef]
15. Goda, K.; Song, J. Uncertainty modeling and visualization for tsunami hazard and risk mapping: A case study for the 2011 Tohoku earthquake. *Stoch. Environ. Res. Risk Assess.* **2015**, *30*, 2271–2285. [CrossRef]
16. González, M.; Álvarez-Gómez, J.A.; Aniel-Quiroga, Í.; Otero, L.; Olabarrieta, M.; Omira, R.; Luceño, A.; Jelinek, R.; Krausmann, E.; Birkman, J.; et al. Probabilistic Tsunami Hazard Assessment in Meso and Macro Tidal Areas. Application to the Cádiz Bay. *Spain. Front. Earth Sci.* **2021**, *9*, 591383. [CrossRef]
17. Omira, R.; Baptista, M.A.; Matias L. Probabilistic Tsunami Hazard in the Northeast Atlantic from Near-and Far-Field Tectonic Sources. *Pure Appl. Geophys.* **2015**, *172*, 901–920. [CrossRef]
18. Omira, R.; Matias, L.; Baptista, M.A. Developing an event-tree probabilistic tsunami inundation model for NE Atlantic coasts: Application to a case study. *Pure Appl. Geophys.* **2016**, *173*, 3775–3794. [CrossRef]
19. Basili, R.; Brizuela, B.; Herrero, A.; Iqbal, S.; Lorito, S.; Maesano, F.E.; Murphy, S.; Perfetti, P.; Romano, F.; Scala, A.; et al. The Making of the NEAM Tsunami Hazard Model 2018 (NEAMTHM18). *Front. Earth Sci.* **2021**, *8*, 616594. [CrossRef]
20. Gopinathan, D.; Heidarzadeh, M.; Guillas, S. Probabilistic quantification of tsunami current hazard using statistical emulation. *Proc. R. Soc. A* **2021**, *477*, 20210180. [CrossRef]
21. Salmanidou, D.M.; Beck, J.; Pazak, P.; Guillas, S. Probabilistic, high-resolution tsunami predictions in northern Cascadia by exploiting sequential design for efficient emulation. *Nat. Hazards Earth Syst. Sci.* **2021**, *21*, 3789–3807. [CrossRef]
22. Instituto Geológico y Minero de España QAFI v.4: Quaternary-Active Faults Database of Iberia (2022). Version 3. Available online: http://info.igme.es/qafi (accessed on 20 April 2022).
23. García-Mayordomo, J.; Insua-Arévalo, J.M.; Martínez-Díaz, J.J.; Jiménez-Díaz, A.; Martín-Banda, R.; Martín-Alfageme, S.; Álvarez-Gómez, J.A.; Rodríguez-Peces, M.; Pérez-López, R.; Rodríguez-Pascua, M.A.; et al. The Quaternary Faults Database of Iberia (QAFI v.2.0). *J. Iber. Geol.* **2012**, *38*, 285–302. [CrossRef]
24. García-Mayordomo J.; Martín-Banda R.; Insua-Arévalo J.M.; Álvarez-Gómez, J.A.; Martínez-Díaz, J.J.; Cabral, J. Active fault databases: building a bridge between earthquake geologists and seismic hazard practitioners, the case of the QAFI v.3 database. *Nat. Hazards Earth Sci. Syst.* **2017**, *17*, 1447–1459. [CrossRef]
25. Martínez-Loriente, S.; Gràcia, E.; Bartolome, R.; Sallarés, V.; Connors, C.; Perea, H.; Lo Iacono, C.; Klaeschen, D.; Terrinha, P.; Dañobeitia J.J.; et al. Active deformation in old oceanic lithosphere and significance for earthquake hazard: Seismic imaging of the Coral Patch Ridge area and neighboring abyssal plains (SW Iberian Margin). *Geochem. Geophys. Geosyst.* **2013**, *14*, 2206–2231. [CrossRef]
26. Martínez-Loriente, S.; Gràcia, E.; Bartolome, R.; Perea, H.; Klaeschen, D.; Dañobeitia, J.J.; Zitellini, N.; Wynn, R.B.; Masson, D.G. Morphostructure, tectono-sedimentary evolution and seismic potential of the Horseshoe Fault, SW Iberian Margin. *Basin Res.* **2018**, *30*, 382–400. [CrossRef]
27. Ramos, A.; Fernández, O.; Terrinha P.; Muñoz, J.A. Neogene to recent contraction and basin inversion along the Nubia-Iberia boundary in SW Iberia. *Tectonics* **2017**, *36*, 257–286. [CrossRef]
28. Serra, C.S.; Martínez-Loriente, S.; Gràcia, E.; Urgeles, R.; Vizcaino, A.; Perea, H.; Bartolome, R.; Pallàs, R.; Lo Iacono, C.; Diez, S.; et al. Tectonic evolution, geomorphology and influence of bottom currents along a large submarine canyon system: The São Vicente Canyon (SW Iberian margin). *Mar. Geol.* **2020**, *426*, 106219. [CrossRef]
29. Proceedings of the IGME and UMA Expert Meeting on Tsunamigenic Sources with Potential Impact in the Iberian Coast, Balearic and Canary Islands, Málaga, Spain, 6–7 November 2017. Available online: https://eventos.uma.es/event_detail/9535/detail/expert-meeting-on-tsunamigenic-sources-with-potential-impact-in-the-iberian-coast-balearic-and-cana.html (accessed on 1 March 2022).
30. Pedrera, A.; Ruiz Constán, A.; Galindo Zaldívar, J.; Chalouan, A.; Sanz de Galdeano, C.; Marín Lechado, C.; Ruano, P.; Benmakhlouf, M.; Akil, M.; López Garrido, A.C.; et al. Is there an active subduction beneath the Gibraltar orogenic arc? Constraints from Pliocene to present-day stress field. *J. Geodyn.* **2011**, *52*, 83–96. [CrossRef]
31. Instituto Geográfico Nacional Centro de Descargas. Available online: https://centrodedescargas.cnig.es/CentroDescargas/index.jsp (accessed on 1 March 2022).
32. European Marine Observation and Data Network Bathymetry Page. Available online: https://www.emodnet-bathymetry.eu/data-products (accessed on 1 March 2022).
33. General Bathymetric Chart of the Oceans Gridded Bathymetry Data Page. Available online: https://www.gebco.net/data_and_products/gridded_bathymetry_data/ (accessed on 1 March 2022).
34. Okada, Y. Surface deformation due to shear and tensile faults in a half-space. *Bull. Seismol. Soc. Am.* **1985**, *75*, 1135–1154. [CrossRef]
35. Kajiura, K. The leading wave of tsunami. *Bull. Earthq. Res. Inst. Tokyo Univ.* **1963**, *41*, 535–571. [CrossRef]
36. Saltelli, A.; Ratto, M.; Andres, T.; Campolongo, F.; Cariboni, J.; Gatelli, D.; Saisana, M.; Tarantola, S. *Global Sensitivity Analysis. The Primer*; John Wiley & Sons Ltd.: West Sussex, UK, 2008; ISBN 978-0470059975.
37. Macdonald, I.A. Comparison of sampling techniques on the performance of Monte-Carlo based sensitivity analysis. In Proceedings of the 11th International IBPSA Building Simulator, Glasgow, Scotland, 27–30 July 2009.
38. Burhenne, S.; Dirk, J.; Gregor, P.H. Sampling based on Sobol′ sequences for Monte Carlo techniques applied to building simulations. In Proceedings of the 12th IBPSA Building Simulator, Sydney, Australia, 14–16 January 2011.

39. Snelling, B.; Neethling, S.; Horsburgh, K.; Collins, G.; Piggott, M. Uncertainty Quantification of Landslide Generated Waves Using Gaussian Process Emulation and Variance-Based Sensitivity Analysis. *Water* **2020**, *12*, 416. [CrossRef]
40. George, D.L.; LeVeque, R.L. Finite volume methods and adaptive refinement for global tsunami propagation and local inundation. *Sci. Tsunami Hazards* **2006**, *24*, 319–328.
41. Qin, X.; Motley, M.; LeVeque, R.; Gonzalez, F.; Mueller, K. A comparison of a two-dimensional depth-averaged flow model and a three-dimensional RANS model for predicting tsunami inundation and fluid forces. *Nat. Hazards Earth Syst. Sci.* **2018**, *18*, 2489–2506. [CrossRef]
42. Berger, M.J.; LeVeque, R.J. Adaptive mesh refinement using wave-propagation algorithms for hyperbolic systems. *SIAM J. Numer. Anal.* **1998**, *35*, 2298–2316. [CrossRef]
43. LeVeque, R.J.; George, D.L.; Berger, M.J. Tsunami modelling with adaptively refined finite volume methods. *Acta Numer.* **2011**, *20*, 211–289. [CrossRef]
44. Delis, A.I.; Mathioudakis, E.N. A finite volume method parallelization for the simulation of free surface shallow water flows. *Math. Comput. Simul.* **2009**, *79*, 3339–3359. [CrossRef]
45. Pophet, N.; Kaewbanjak, N.; Asavanant, J.; Ioualalen, M. High grid resolution and parallelized tsunami simulation with fully nonlinear Boussinesq equations. *Comput. Fluids* **2011**, *40*, 258–268. [CrossRef]
46. Brodtkorb, A.; Hagen, T.; Lie, K.; Natvig, J. Simulation and visualization of the Saint-Venant system using GPUs. *Comput. Vis. Sci.* **2010**, *13*, 341–353. [CrossRef]
47. Asunción, M.; Mantas, J.; Castro, M. Programming CUDA-Based GPUs to Simulate Two-Layer Shallow Water Flows. In Proceedings of the 16th International Euro-Par Conference, Ischia, Italy, 31 August–3 September 2010; pp. 353–364.
48. Amouzgar, R.; Liang, Q.; Smith, L. A GPU-accelerated shallow flow model for tsunami simulations. *Proc. Inst. Civ. Eng. Eng. Comput. Mech.* **2014**, *167*, 117–125. [CrossRef]
49. Amouzgar, R.; Liang, Q.; Clarke, P.; Yasuda, T.; Mase, H. Computationally Efficient Tsunami Modelling on Graphics Processing Units (GPU). *Int. J. Offshore Polar Eng.* **2017**, *26*, 154–160. [CrossRef]
50. Castro, M.J.; Ferreiro, A.; García, J.A.; González, J.M.; Macías, J.; Parés, C.; Vázquez, M.E. On the numerical treatment of wet/dryfronts in shallow flows: Applications to one-layer and two-layer systems. *Math. Comp. Model* **2005**, *42*, 419–439. [CrossRef]
51. Castro, M.J.; González, J.M.; Parés, C. Numerical treatment of wet/dry fronts in shallow flows with a modified Roe scheme. *Math. Mod. Meth. App. Sci.* **2006**, *16*, 897–931. [CrossRef]
52. Castro, M.J.; Chacón, T.; Fernández-Nieto, E.D.; González-Vida, J.M.; Parés, C. Well-balanced finite volume schemes for 2D non-homogeneous hyperbolic systems. Applications to the dam break of Aznalcóllar. *Comp. Meth. Appl. Mech. Eng.* **2008**, *197*, 3932–3950. [CrossRef]
53. Asunción, M.; Castro, M.J.; Fernández-Nieto, E.D.; Mantas, J.M.; Ortega, S.; González-Vida, J. M. Efficient GPU implementation of a two waves TVD-WAF method for the two-dimensional one layer shallow water system on structured meshes. *J. Comput. Fluids* **2013**, *80*, 441–452. [CrossRef]
54. Gallardo, J.M.; Parés, C.; Castro, M. On a well-balanced high-order finite volume scheme for shallow water equations with topography and dry areas. *J. Comp. Phys.* **2007**, *227*, 574–601. [CrossRef]
55. Macías, J.; Castro, M.J.; Escalante, C. Performance assessment of Tsunami-HySEA model for NTHMP tsunami currents benchmarking. Laboratory data. *Coast. Eng.* **2020**, *158*, 103667. [CrossRef]
56. Macías, J.; Castro, M.J.; Ortega, S.; González-Vida, J.M. Performance assessment of Tsunami-HySEA model for NTHMP tsunami currents benchmarking. Field cases. *Ocean Model* **2020**, *152*, 101645. [CrossRef]
57. Macías, J.; Castro, M.J.; Ortega, S.; Escalante, C.; González-Vida, J.M. Performance benchmarking of Tsunami-HySEA model for NTHMP's inundation mapping activities. *Pure Appl. Geophys.* **2017**, *174*, 3147–3183. [CrossRef]
58. Aki, K. Generation and propagation of G waves from Niigata earthquake of June 16, 1964. Part 2. Estimation of earthquake moment, released energy, and stress-strain drop from the G wave spectrum. *Bull. Earthq. Res. Inst.* **1966**, *44*, 73–88. [CrossRef]
59. Hanks, T.C.; Kanamori, H. A moment magnitude scale. *J. Geophys. Res.* **1979**, *84*, 2348–2350. [CrossRef]
60. Stirling, M.; Goded, T.; Berryman, K.; Litchfield, N. Selection of earthquake scaling relationships for seismic-hazard analysis. *Bull. Seismol. Soc. Am.* **2013**, *103*, 2993–3011. [CrossRef]
61. Fisher, N.I.; Lewis, T.; Embleton, B.J. *Statistical Analysis of Spherical Data*; Cambridge University Press: Cambridge, UK, 1993; ISBN 9780521456999.
62. Jammalamadaka, S.R.; Sengupta, A. *Topics in Circular Statistics*; World Scientific: Singapore, 2001; Volume 5, ISBN 9789810237783.
63. Mardia, K.V.; Jupp, P.E. *Directional Statistics*; John Wiley & Sons: Chichester, UK, 2009; Volume 494, ISBN 9780471953333.
64. Devroye, L. *Non-Uniform Random Variate Generation*; Springer: New York, NY, USA, 1986; ISBN 978-1-4613-8645-2.
65. Schneider, B.; Hoffmann, G.; Reicherter, K. Scenario-based tsunami risk assessment using a static flooding approach and high-resolution digital elevation data: An example from Muscat in Oman. *Glob. Planet. Chang.* **2016**, *139*, 183–194. [CrossRef]
66. Okumura, N.; Jonkman, S.N.; Esteban, M.; Hofland, B.; Shibayama, T. A method for tsunami risk assessment: A case study for Kamakura, Japan. *Nat. Hazards* **2017**, *88*, 1451–1472. [CrossRef]
67. Rose, A.; Sue Wing, I.; Wei, D.; Wein, A. Economic impacts of a California tsunami. *Nat. Hazards Rev.* **2016**, *17*, 04016002. [CrossRef]
68. Geist, E.; Parsons, T. Probabilistic analysis of tsunami hazards. *Nat. Hazards* **2006**, *37*, 277–314. [CrossRef]

69. Zamora, N.; Babeyko, A.Y. Probabilistic tsunami hazard assessment for local and regional seismic sources along the Pacific coast of Central America with emphasis on the role of selected uncertainties. *Pure Appl. Geophys.* **2020**, *177*, 1471–1495. [CrossRef]
70. Griffin, J.; Pranantyo, I.R.; Kongko, W.; Haunan, A.; Robiana, R.; Miller, V.; Davies, G.; Horspool, N.; Maemunah, I.; Widjaja, W.B.; et al. Assessing tsunami hazard using heterogeneous slip models in the Mentawai Islands, Indonesia. *Geol. Soc. Spec.* **2016**, *441*, 47–70. [CrossRef]
71. El-Hussain, I.; Omira, R.; Deif, A.; Al-Habsi, Z.; Al-Rawas, G.; Mohamad, A.; Al-Jabri, K.; Baptista, M.A. Probabilistic tsunami hazard assessment along Oman coast from submarine earthquakes in the Makran subduction zone. *Arab. J. Geosci.* **2016**, *9*, 668. [CrossRef]